UNIVERSITÀ DEGLI STUDI DI PADOVA

MASTER'S THESIS

Exploring the relationship between multi-scale functional dynamics and cerebral protein synthesis measured with L-[1-^{11}C]Leucine PET

Author:
Alberto PELLIZZON

Supervisor:
Prof. Alessandra BERTOLDO
Co-supervisors:
Dr. Gaia RIZZO
Dr. Mattia VERONESE

A work from the collaboration between
Department of Information Engineering

and

Department of Neuroimaging, King's College London

April 19, 2016


UNIVERSITAS STUDII PADUANI
MCCXXII


DEPARTMENT OF
INFORMATION
ENGINEERING
UNIVERSITY OF PADOVA


KING'S College LONDON
Institute of
Psychiatry, Psychology
& Neuroscience

UNIVERSITÀ DEGLI STUDI DI PADOVA

Abstract

Scuola di Ingegneria
Department of Information Engineering

Laurea Magistrale in Bioingegneria

Exploring the relationship between multi-scale functional dynamics and cerebral protein synthesis measured with L-[1-^{11}C]Leucine PET

by Alberto PELLIZZON

Introduction: In recent years, graph theory seems to be the most appealing way to model and investigate brain connectivity, yet theoretical measures do not have a straightforward biological interpretation. Recently, L-[1-^{11}C]Leucine PET has been used to objectively measure in vivo protein synthesis in the cortex (Veronese et al., 2012). However, the relationship between regional protein synthesis and on-going neural dynamics is unclear. We use a graph theoretical approach (Bullmore and Sporns, 2009), to examine the relationship between functional connectivity (measured using fMRI) and the rate of cerebral protein synthesis (rCPS).
Methods: We used resting state functional MRI (R-fMRI) from 20 healthy subjects (Age: 23-33) derived from the Human Connectome Project 'FIX' pipeline (Van Essen et al., 2013). R-fMRI was filtered in a broad frequency band between 0.001 and 0.62 Hz. Functional connectivity (FC) matrices were generated using three different brain anatomical atlases (AAL (Tzourio-Mazoyer et al., 2002), Craddock 200 (Craddock et al., 2012), and Freesurfer (Fischl, 2012)). Group level FC matrices were then thresholded in order to maximize cost-efficiency (Bassett et al., 2009), before calculating six graph theoretical measures of centrality, using the Brain Connectivity Toolbox (Rubinov and Sporns, 2010). Age matched L-[1-^{11}C]Leucine and [^{18}F]FDG PET templates were derived from previously published studies (Bishu et al., 2008) and were segmented using the same parcellation schemes as the MRI data.
Results: Using a filter-bank approach, we firstly demonstrated a significant relationship between protein turnover (measured using L-[1-^{11}C]Leucine PET) and graph theoretical measures of functional connectivity. Moreover, this relationship was significantly modulated by temporal scale, where dynamics with a temporal frequency of 0.06-0.12 Hz were producing stronger

correlations. To assess how these relationships may be driven simply by enhanced metabolism within hub-regions in the brain, we performed similar analysis using [^{18}F]FDG binding patterns. Whilst some relationship between FDG binding and graph theoretical measures was present, when included as a covariate in the relationship between L-[1-^{11}C]Leucine and functional connectivity, there remained a significant relationship between protein turnover and graph theoretical measures. Results were consistent for the different atlases.

We also used a sliding window approach to split R-fMRI scans into shorter consecutive time-series, and found that protein synthesis was inversely correlated with the variability of theoretical network measures, suggesting greater stability in hub regions.

Conclusion: With this work we demonstrate using a combined fMRI and PET approach that cerebral protein synthesis has a strong relationship to neural dynamics at the macroscopic scale. The association between the two appears to be dependent to the temporal scale of fMRI signal, and independent from tissue metabolism.

Acknowledgements

The realisation of the present work was possible thanks to my family, which supported me through the years. I would also like to thank my supervisor Alessandra Bertoldo, and co-supervisors Gaia Rizzo and Mattia Veronese, as they were present whenever I needed some help. Thanks also to Peter John Hellyer and Erica Barry for their previous work on the topics covered by this thesis. A special thanks to my friends and to all the people - at the Department of Information Engineering and at the Centre for Neuroimaging Sciences - that made easier to go through the production of this work.

Contents

List of Abbreviations

AM	Adjacency Matrix
BOLD	Blood Oxygenation Level Dependent
CM	Correlation Matrix
CV	Coefficient of Variation
DVR	Distribution Volume Ratio
FC	Functional Connectivity
FDG	Fluorodeoxyglucose
GM	Grey Matter
HCP	Human Connectome Project
ICA	Independent Component Analysis
MNI	Montreal Neurological Institute
MRI	Magnetic Resonance Imaging
– dMRI	Diffusion MRI
– fMRI	Functional MRI
– R-fMRI	Resting State fMRI
PET	Positron Emitting Tomography
PiB	Pittsburgh Compound B
rCPS	Regional Cerebral Protein Synthesis
ROI	Region of Interest
SC	Structural Connectivity
SD	Standard Deviation
SUV	Standardized Uptake Value
TAC	Time-Activity Curve
WM	White Matter

Chapter 1

Introduction

Neuroimaging is a relatively recent, and rapidly expanding discipline that plays a relevant role in medicine, psychology and neuroscience in general. Neuroimaging aims to unravel the complexities of the central nervous system, by obtaining and studying images that represent brain structures or functions (Filler, 2009). Scanning methods include magnetic resonance imaging (MRI) and positron emission tomography (PET), in the attempt to quantify structural, functional, and effective qualities of the brain *in vivo*. The interest of many research groups all across the world, together with technological advance, is permitting this discipline to grow and develop day by day. In particular, in the last two decades, MRI has come to dominate the brain mapping field, thanks to lack of radiation exposure, low invasiveness and wide availability.

There is however an open debate over which imaging methods and models provide the most biologically meaningful measures in the human brain. The most widely used model is based on graph theory, the mathematical method of representing real world phenomena using nodes/vertices and edges/links (Rubinov and Sporns, 2010). The basis of graph theory suggests that different complex systems use the same organisational principles and can therefore be quantified by the same parameters (Bullmore and Sporns, 2009). Adopting this model, we assume that the brain is one large entity that is shaped by local and global connectional organisation, such as the density of connections, clustering, and efficiency (Hagmann et al., 2010). Graph theory utilises different measures to highlight important qualities about that network such as the integration, segregation, and small-world connectivity (Latora and Marchiori, 2001; Sporns and Zwi, 2004).

Neural network analysis has been used to investigate various aspects of neural dynamics in the brain. It has been used to compare healthy controls to patients with psychological illnesses, such as autism, depression, and schizophrenia, as well as the effects of ageing in the brain. Studies suggested that a network disruption, hypo-activity, or hyperactivity could underpin many of the brain disorders typically seen in clinic and research (Olde Dubbelink et al., 2013; Cherkassy et al., 2006; Kleberg, 2014). Other applications of network analysis and graph theory include more theoretical

and exploratory studies which try to disentangle the relationship between structural, functional, and cellular level networks, and build potential computational models of neural dynamics at different scales (He et al., 2010; Deng and Zhang, 2007; Massobrio, Pasquale, and Martinoia, 2015; Monti et al., 2014).

PET and functional MR (fMRI) studies seem to agree on some basic aspects of the brain as a network, such as the existence of central hubs and small-world properties (Sporns and Zwi, 2004; Massobrio, Pasquale, and Martinoia, 2015; Deng and Zhang, 2007). However, when considering real world networks, complications emerge, as those are typically large, complex, and are not uniformly ordered or random (Rubinov and Sporns, 2010). To explain this, many researchers proposed that those networks must have scale-free properties (He et al., 2010; Deng and Zhang, 2007; Monti et al., 2014). The most notable characteristic in a scale-free network is the common presence of nodes with a degree (number of connections) that greatly exceeds the average, referred to as "hubs". Also the scale-free property relates strongly with the network's robustness to failure. In a scale-free model the time scale being investigated should demonstrate the same principles as the other time scales, but this is not always the case, and it is difficult to distinguish key signal in fMRI due to artefacts and noise. This notion makes determining functional connectivity particularly difficult as there are many different time scales occurring simultaneously in a fMRI scan (Monti et al., 2014). Connection observations could therefore be a sum of the different time scales occurring. To overcome this, researchers have begun separating different frequencies during analyses, and have found that different time scales have significant differences on the connectivity matrices produces from this analysis (He et al., 2010; Deng and Zhang, 2007; Massobrio, Pasquale, and Martinoia, 2015; Monti et al., 2014). For example low frequency fluctuations (LFF, <0.1 Hz), which are typically examined in resting state MRI (R-fMRI), are characterized by synchronous spontaneous fluctuations that occur between lower and higher order regions, forming what is now termed the "default mode network" (DMN) (Raichle et al., 2001).

Many recent studies have shown that the supposed period of rest that occurs when the brain is not directly stimulated, behaved as a network as well (Ponce-Alvarez et al., 2015). This led to investigate the resting state of the brain by imaging during no explicit stimulation. Many studies have found that underlying psychiatric illnesses and pathologies have differing resting state networks (RSN) when compared with healthy controls, indicating that differences occur in this network, possibly affecting the brain's overall capacity to function.

The dynamic changes in the RSN led to new theories such as the brain as a critical system, functioning in a metastable state in order to be able to adapt

to internal and external stimuli (Rubinov et al., 2011; Monti et al., 2014; Massobrio, Pasquale, and Martinoia, 2015). Such ability to reorganize and form new neural connections is referred to as neuroplasticity, a complex yet fundamental process in brain development.

In order to effectively interact with the external world, the brain must build rich representations of environmental inputs received from sensory systems and update these representations ensuing action plans to effectively interact with a dynamic environment. Over 50 years ago, Flexner and colleagues showed that injections of puromycin, a protein synthesis inhibitor, into the mouse brain from 1 to 3 days after learning blocked the animal's ability to remember the location of a shocked arm in a Y-maze (Flexner, Flexner, and Stellar, 1963). Thus consolidation of memory requires not only modifications to existing proteins but also changes in "de novo" protein synthesis.

As introduced before, evidence has been reported that the brain is functionally organized as a complex system possessing a critical attractor (Massobrio, Pasquale, and Martinoia, 2015; Hesse and Gross, 2014). A system at a "critical state" is finely balanced in a position between robust ordered and chaotic dynamics (Rubinov et al., 2011). Such dynamics are attractive as a model for neural function, as they provide a mechanistic framework for storage and processing information in a fluid dynamic system. Moreover the theoretically useful, "critical" dynamics which may underpin memory and consolidation processes, may in part be supported not just by the interaction between regions, but also by localized plasticity. Homeostatic plasticity, alongside a range of other adaptive or plastic approaches, have been proposed as a potential tuning mechanism for maintaining "critical" neural dynamics. (Cowan et al., 2013; Magnasco, Piro, and Cecchi, 2009; Meisel and Gross, 2009). In the brain, these plastic mechanisms may not only induce critical dynamics, but also enhance the emergence of functional connectivity networks. A full understanding of functional connectivity therefore must also include not only measures of structure and functional connectivity, but a frank understanding on how protein synthesis in the brain relates to functional integration.

In this work, we use a graph theoretical approach to examine the relationship between functional connectivity (measured using fMRI) and objective measures of protein synthesis. The L-[1-^{11}C]Leucine PET method allows the quantitative determination of local rates of protein synthesis in the central nervous system *in vivo*. This assay uses L-[1-^{11}C]Leucine as a tracer to measure the rate of incorporation of leucine, one of the nine essential amino acids, into protein. Leucine is very attractive for this kind of assay because its only pathway of degradation is transamination followed by carboxylation; here the ^{11}C label is quickly transferred to labelled CO_2 which is quantitatively minimal and negligibly re-incorporated as heavily

diluted by the large pool of unlabelled CO_2 resulting from carbohydrate metabolism. Hence brain radioactivity is mostly due to free [^{11}C] leucine and labelled protein defining a sympathetic measure of "de novo" cerebral protein synthesis (rCPS) (Smith et al., 2005; Schmidt et al., 2005). Applied to the human-brain this approach allows the quantification of regional plasticity in the cortex. We start by relating functional connectivity to structure, demonstrating similar results to those described previously that structural connectivity is best predictive of function at a slow temporal scale (Park and Friston, 2013). Next, we explore the hypothesis that large-scale dynamics of the brain are in part constrained empirically by plasticity at a broad range of temporal scales using both a temporal filtering and dynamic sliding window functional connectivity approach. Specifically, we relate graph theoretical measures of the brain with rCPS measured using L-[1-^{11}C]Leucine PET. Furthermore, we compare and contrast these results with a simpler description of functional processing using Fluorodeoxyglucose ([^{18}F]FDG) PET as a proxy measure of node synaptic activity, as more than 85% of cerebral glucose is used by neurons and mainly by presynaptic axon terminals. The brain uses myelination to set boundaries to network plasticity; these boundaries appear to be looser for local networks, that are wired through high frequency activity, and less so for long-distance hubs that are characterized by transmission on low-frequency band. This phenomenon has been described as "meta-plasticity", studied in pre-clinical and computational models but never before demonstrated in human brain networks. Hence we have also hypothesized that rCPS would show association to graph theoretical measures that would vary with the frequency range of fMRI oscillations with the association being stronger on low-frequency bands. We also hypothesise that there will be a significant relationship between functional connectivity network measures and protein synthesis, and that this relationship will not fade if we take into account metabolism as a confounding factor. Plus, by finding any significant difference between temporal filtering bands, our findings could imply that underlying power law dynamics may potentially influence or govern complex neural dynamics.

Chapter 2

Materials and Methods

2.1 Datasets

In the present work we considered four different datasets:

- L-[1-^{11}C]Leucine PET as biomarker of cerebral protein synthesis
- [^{18}F]FDG PET as biomarker of glucose metabolism
- Resting-state fMRI to measure functional connectivity
- Diffusion MR to measure structural connectivity

A summary of the datasets is reported in Figure 2.1. All studies obtained informed consent and were approved by their respective medical ethics committees in line with the Declaration of Helsinki. All participants had no history of neurological or psychiatric disorders.

2.1.1 Magnetic Resonance

Data were provided by Human Connectome Project (HCP) (humanconnectome.org/), in particular they come from the 500 Subjects + MEG2 release (Mapping, 2014). Between all the available subjects, we randomly chose 20 of them, 10 male and 10 female, with an average age of 30.05 years old, and standard deviation 3.30. No other constraints except from age and sex were applied. Both resting-state (R-fMRI) and diffusion (dMRI) data come from the same set of subjects.
All HCP subjects were scanned on a customized Siemens 3T "Connectome Skyra" housed at Washington University in St. Louis, using a standard 32-channel Siemens receive head coil and a "body" transmission coil designed by Siemens specifically for the smaller space available using the special gradients of the WU-Minn and MGH-UCLA Connectome scanners. For more information on the customizations made on the hardware, refer to the HCP documentation (Mapping, 2014).

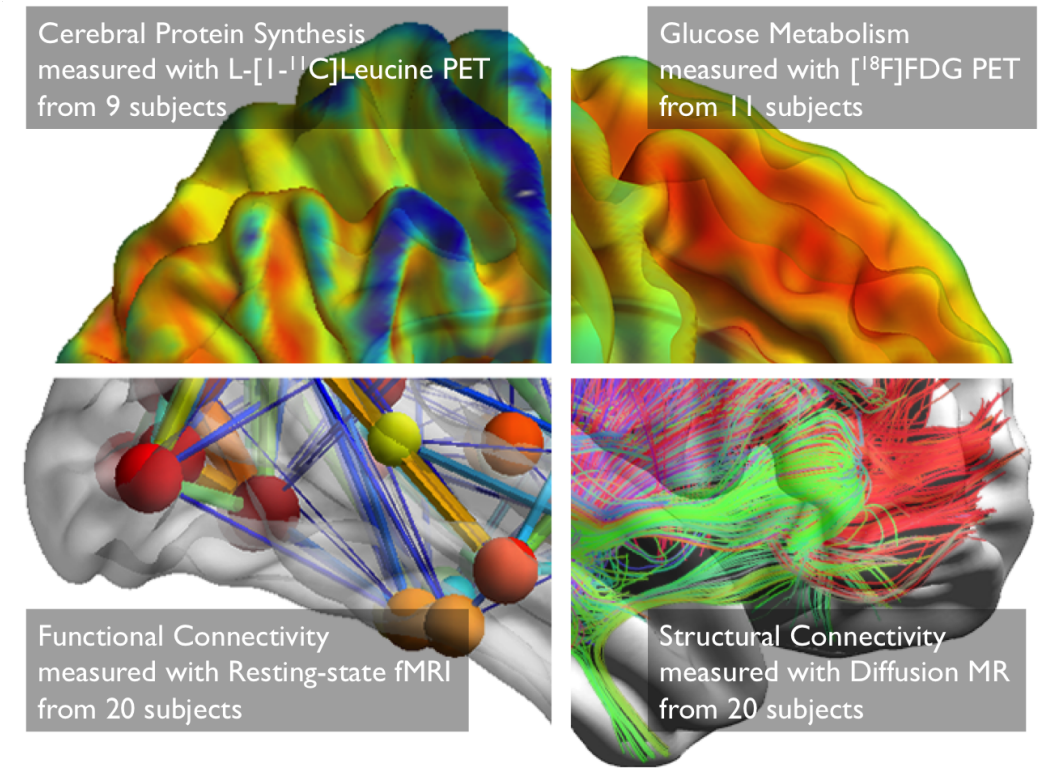

FIGURE 2.1: Overview of the datasets used for this study

Resting-state fMRI (R-fMRI)

Data were acquired in four runs of approximately 15 minutes each, with eyes open with relaxed fixation on a projected bright cross-hair on a dark background (and presented in a darkened room). The four runs were divided into two sessions, with oblique axial acquisitions alternating between phase encoding in a right-to-left (RL) direction in one run and phase encoding in a left-to-right (LR) direction in the other run. We used datasets belonging to first sessions, and runs labelled LR. Images were acquired with the parameters listed in Table 2.1, a total of 1200 slices were obtained for each run (duration 14:33 minutes).

Diffusion imaging (dMRI)

The hardware modifications mentioned above, that were made on the Siemens 3 T Skyra system, notably improve diffusion imaging (Sotiropoulos et al., 2013). A full dMRI session included 6 runs (each approximately 9 minutes and 50 seconds), representing 3 different gradient tables, with each table acquired once with right-to-left and left-to-right phase encoding polarities, respectively. Each gradient table included approximately 90 diffusion weighting directions plus 6 b=0 acquisitions interspersed throughout each run. Diffusion weighting consisted of 3 shells of b=1000, 2000, and

Sequence	Gradient-echo EPI
TR	720 ms
TE	33.1 ms
flip angle	52°
FOV	208×180 mm (RO×PE)
Matrix	104×90 (RO×PE)
Slice Thickness	2.0 mm, 72 slices, 2.0 mm isotropic voxels
Multiband factor	8
Echo spacing	0.58 ms
BW	2290 Hz/Px

TABLE 2.1: R-fMRI acquisition details

3000 s/mm^2 interspersed with an approximately equal number of acquisitions on each shell within each run. Detailed specifications are reported in Table 2.2.

Sequence	Spin-echo EPI
TR	5520 ms
TE	89.5 ms
flip angle	78°
refocusing flip angle	160°
FOV	210×180 mm (RO×PE)
Matrix	168×144 (RO×PE)
Slice Thickness	1.25 mm, 111 slices, 1.25 mm isotropic voxels
Multiband factor	3
Echo spacing	0.78 ms
BW	1488 Hz/Px
Phase partial Fourier	6/8
b-values	1000, 2000, and 3000 s/mm^2

TABLE 2.2: dMRI acquisition details

2.1.2 Positron Emitting Tomography

L-[1-^{11}C]Leucine

Data from nine healthy awake male subjects (age 20 to 24) from a previous study (Bishu et al., 2008) were used. The criteria for subject inclusion and the procedure for L-[1-^{11}C]Leucine PET studies are described in detail in the original work. All studies were performed on the High-Resolution Research Tomograph (HRRT) (CPS Innovations, Knoxville, TN, USA), which has spatial resolution of 2.6 mm full width at half maximum (Wienhard et al., 2002). L-[1-^{11}C]Leucine was prepared from H^{11}CN, and obtained a radiochemical purity of >99% and an estimated specific activity of 3 mCi/nmol.

The 90-min emission scan was initiated coincident with a 2-min intravenous infusion of 20 to 30 mCi of L-[1-^{11}C]Leucine. Estimated leucine-specific activity was 3 mCi/nmol. Images were reconstructed using motion-compensated three-dimensional ordinary Poisson ordered subset expectation maximization as 42 frames (16×15, 4×30, 4×60, 4×150, 14×300 secs); voxel size was 1.21×1.21×1.23 mm. Arterial blood sampling was performed; concentrations of unlabelled and labelled leucine in plasma and total ^{11}C and $^{11}CO_2$ activities in whole blood were measured according to methods detailed in (Bishu et al., 2008). All subjects underwent a T1-weighted magnetic resonance imaging of the brain for ROI placement.

[^{18}F]FDG

Data came from 11 healthy volunteers, 6 male and 5 female, aged 30.5±7.1 years old. Resting-state [^{18}F]FDG PET/CT brain images were acquired in a GE Discovery 690 (GE Healthcare, Milwaukee, Wisconsin, USA), at the Centro de Tecnologia em Medicina Molecular, Faculdade de Medicina da UFMG, Belo Horizonte, Brazil. Subjects had at least six hours of fasting before the exam. After intravenous bolus injection of 5.18 MBq/kg of [^{18}F]FDG, subjects rested for 50 minutes in a quiet and dark room with minimum stimuli. PET brain images were acquired subsequently, with an acquisition time of 10 minutes, and reconstructed in a 192×192×47 matrix using the OSEM (Ordered Subsets Expectation Maximization) algorithm, with 2 iterations and 20 subsets. CT images were used to perform attenuation correction.

2.2 Data pre-processing

2.2.1 Resting-state fMRI (R-fMRI)

Resting-state fMRI data has been cleaned through the use of independent component analysis (ICA) based artefact removal, to remove non-neural spatiotemporal components from each (highpass filtered) run of R-fMRI data. ICA is a powerful approach for decomposition of fMRI data as a summation of "good" and "bad" components, where each component comprises a weighted set of voxels (the component's spatial map), along with a single timeseries that is common to those voxels identified. Once ICA has identified a number of artefactual components, the data can be "cleaned" by subtracting these components from the data.
The approach HCP developed, combined ICA (run using FSL's MELODIC) with a more complex automated component classifier referred to as FIX (FMRIB's ICA-based X-noisifier) that has been specifically trained on HCP

data. The FIX approach and initial results of classification accuracy are described in detail in (Salimi-Khorshidi et al., 2014), and the effects of the ICA + FIX cleanup (and optimal methods to remove the bad components from the data) are evaluated in detail in (Griffanti et al., 2014).

2.2.2 Diffusion MR (dMRI)

Reconstructed dMRI images were used from the standard dHCP pipeline which were corrected for phase-encoding, susceptibility and eddy-current artefacts using 'topup' and 'eddy' from the FSL diffusion toolkit (http://fsl.fmrib.ox.ac.uk/fsl/fslwiki/FDT). dMRI was subsequently analysed using a constrained spherical deconvolution approach, followed by whole-brain probabilistic tractography using MRtrix3 (http://www.mrtrix.org). In brief, for each subject, a fibre orientation density map was generated from the dMRI images which was used to perform probabilistic tractography using the iFOD2 method (Tournier, Calamante, and Connelly, 2010). During the tractography, 10-million streamlines were randomly seeded from the grey-white matter boundary using the MRtrix SIFT algorithm (Smith et al., 2013), resulting in a dense connectogram for the entire brain. A b0 $\rightarrow$ MNI standard space warp-field provided by the HCP, was used to co-register each of the three atlases to the dMRI image space where connectivity matrices were generated using the MRtrix tck2connectome tool, resulting in symmetrical connectivity graphs where each node is an ROI in the atlas and edge is represented by the number of streamlines which passed successfully between each pair of ROIs. These matrices were further manipulated, by dividing each edge by the total number of streamlines emerging from each 'seed' ROI, resulting in a normalised structural connectivity matrix for each subject.

2.2.3 PET quantification

L-[1-^{11}C]Leucine

Leucine PET images were quantified using the Spectral Analysis Iterative filter method (SAIF) (Veronese et al., 2010) as implemented in (Veronese et al., 2012). The method allows parametric imaging for regional cerebral protein sysnthesis (rCPS), accounting for the tracer tissue kinetic heterogeneity and the fraction of unlabelled leucine in the tissue precursor pool for protein synthesis derived from arterial plasma (Schmidt et al., 2005). Individual rCPS maps were normalised to stereotaxic MNI (Montreal Neurological Institute) space via T1 weighted MRI images, and averaged across subjects to generate a template rCPS image (Figure 2.2).

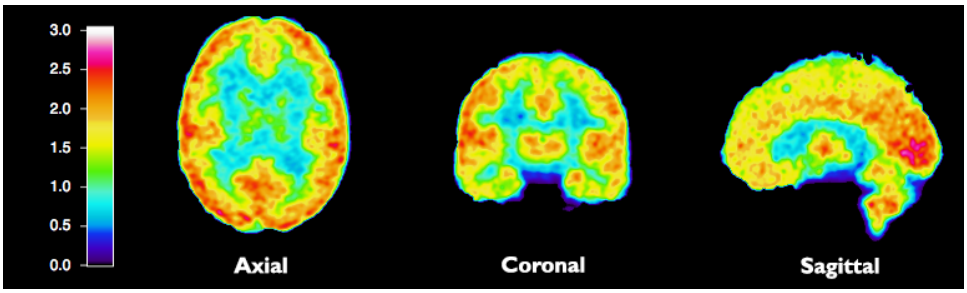

FIGURE 2.2: L-[1-^{11}C]Leucine template (rCPS)

[^{18}F]FDG

For the FDG PET images, the Standardised Uptake Value (SUV) normalised by body weight and injected dose was calculated. SUV is mainly considered as a semi-quantitative measure, yet is easy to compute and its interpretation is straightforward. A SUV template (Figure 2.3) was then built, by averaging individual images in MNI space.

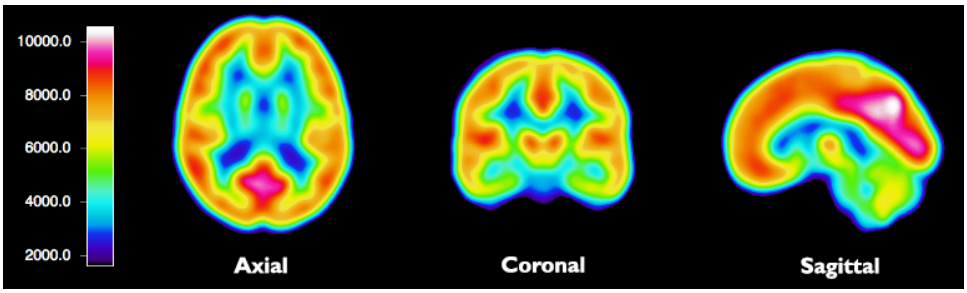

FIGURE 2.3: [^{18}F]FDG SUV template

Chapter 3

Data Analysis

Every step of the analysis was carried out using Matlab, Release 2013a.
The biggest part of the analysis focused on functional and structural MR data. PET data (SUV and rCPS templates) were only segmented following the parcellation schemes discussed below (section 3.1), and used for correlating against MR-derived network measures (section 3.4).
The second chapter, Temporal Filtering, regards only resting state MR data. This technique is based on Blood-oxygen-level dependent contrast imaging, and BOLD signal is still a matter of study, it is in fact affected by a vast quantity of variables, most of them unpredictable, and related both to the scanner and the subject. BOLD signal spectrum is not deeply known, and by introducing temporal filtering, we aim to better understand what kind of information different frequency bands bring.
In 3.1 there is an overview of the analysis pipeline we followed for resting state data.

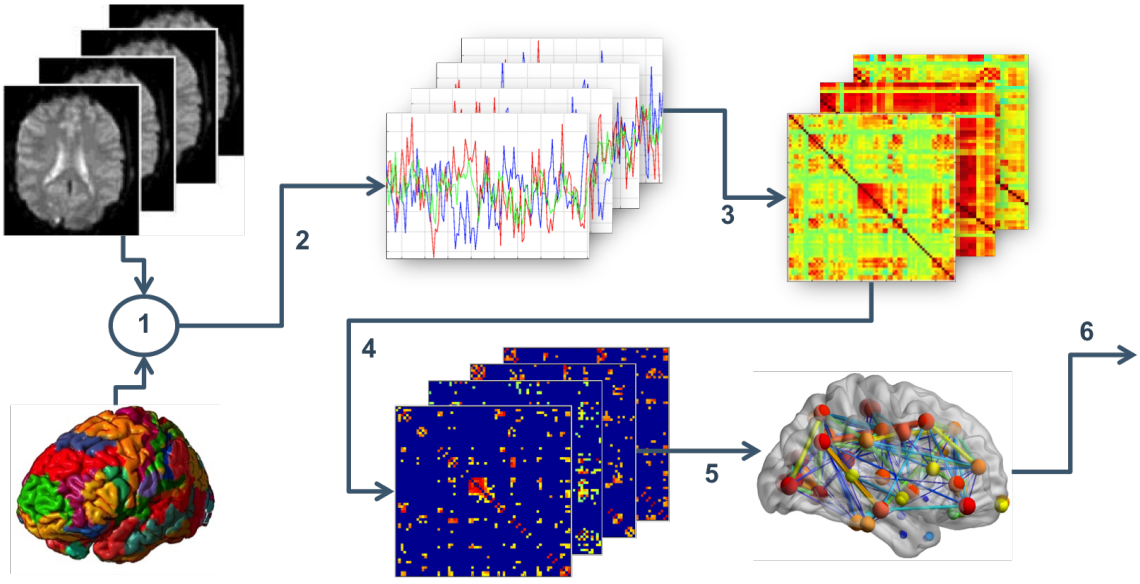

FIGURE 3.1: Resting state data analysis pipeline: 1-segmentation with anatomical atlas 2-temporal filtering 3-correlation matrices construction 4-thresholding and adjacency matrices construction 5-calculation of functional network measures 6-correlations with PET data.

3.1 Segmentation

Three different brain atlases were used to segment data, in order to assess differences between parcellation schemes, and to investigate how they influence results, and also to possibly discard brain parcellations that are not suitable for these kinds of studies.
The first atlas we used is Automated Anatomical Labeling (Tzourio-Mazoyer et al., 2002), an atlas based on the MNI single-subject brain and Statistical Parametric Mapping package (Friston et al., 1995). In particular, we used a version consisting in 67 regions of interest (ROIs). Dividing the whole brain volume into 67 regions, results in a loose anatomical parcellation, as showed in Figure 3.2.
The second atlas we used is the Craddock (Craddock et al., 2012). It is generated with a completely different approach from AAL, in fact the segmentation is thought specifically for resting-state fMRI, and it is fully data-driven. With this approach, brain is divided into spatially coherent regions of functional connectivity. We used the 200 ROIs version, as showed in Figure 3.2.
The last atlas we used is based on FreeSurfer (Fischl, 2012) (`http://surfer.nmr.mgh.harvard.edu`), with 82 ROIs. As we can see in Figure 3.2, this atlas mostly segments cerebral cortex, not focusing on white matter. This is a big difference with respect to the previous atlases. It is also the most widely used in literature for fMRI studies.

3.2 Temporal Filtering

Calculating the average time-activity curve (TAC) between voxels belonging to the same ROIs, we obtained a TAC for each ROI. This signal had a sampling interval of 720 ms (see TR in R-fMRI acquisition specifications, 2.1.1). Such sampling correspond to a Nyquist frequency (the highest frequency we are able to distinguish in a sampled signal) of 0.694 Hz. Because of our large frequency span, with respect to previous studies, and knowing that different frequencies bring different information, we filtered TACs using 20 overlapping bands. As showed in Figure 3.3 we used tighter bands at low frequencies, in order to better examine low frequency fluctuations in the BOLD signal, as they represent the most prominent part of it (He et al., 2010). This can also be seen in Figure 3.4. We implemented a digital raised-cosine bandpass filter (mathematical description at `http://commsys.isy.liu.se/TSKS04/lectures/3/MichaelZoltowski_SquareRootRaisedCosine.pdf`), with 0.005 Hz transition bands centred at cut-off frequencies, whose values can be found in Appendix A.

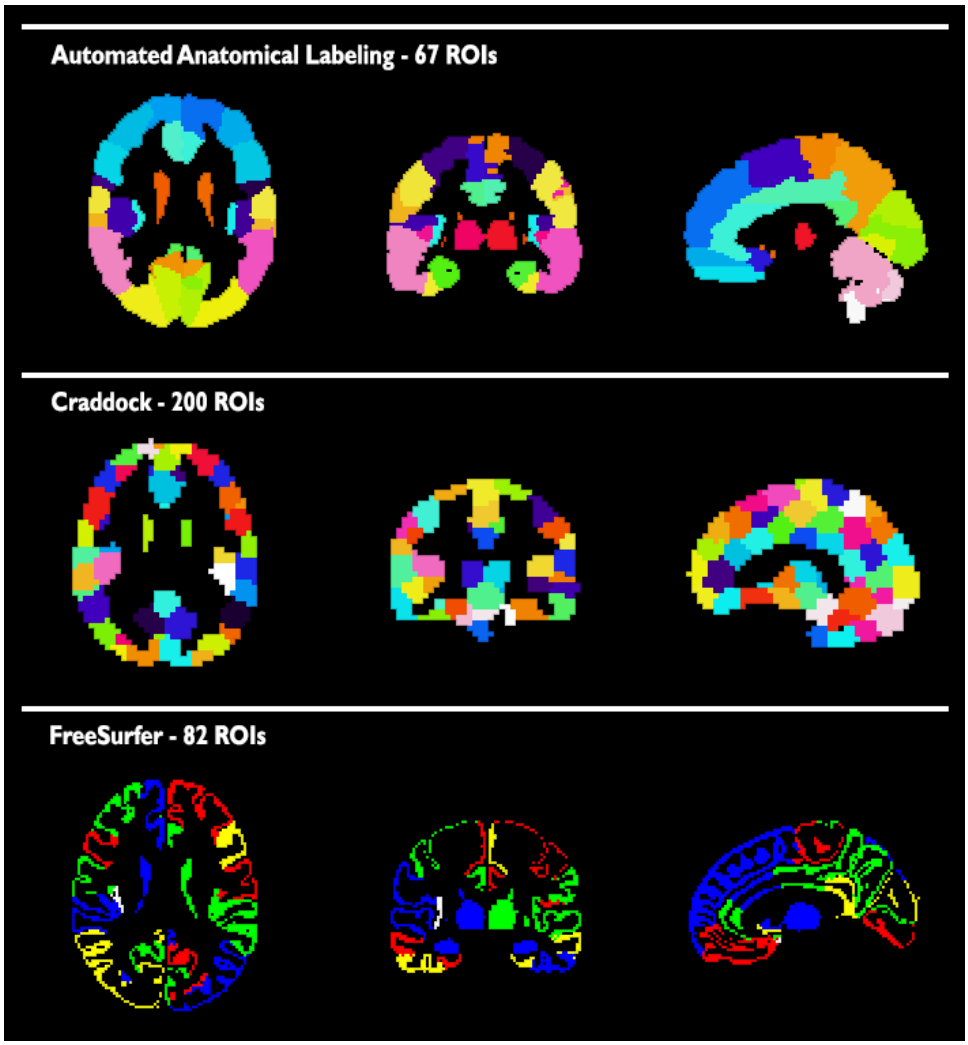

FIGURE 3.2: the three brain anatomical atlases used in this study.

However we report in the results only frequencies up to 0.3 Hz, regarding the first twelve frequency bands, we do this for clarity, as our main findings are mainly situated ad low frequencies. Complete results, covering the whole frequency spectrum, can be found in Appendix A.

3.3 Network Construction

3.3.1 R-fMRI

In order to conduct our study through graph theory (or more precisely a part of it, network theory), we have to define nodes (or vertices) and edges. Ideally, nodes would be neurons or groups of them, but technology does not currently allow it, and also analysis at voxel level would include too much noise, and would also require huge computational capabilities. So nodes, our interactive units, are represented by groups

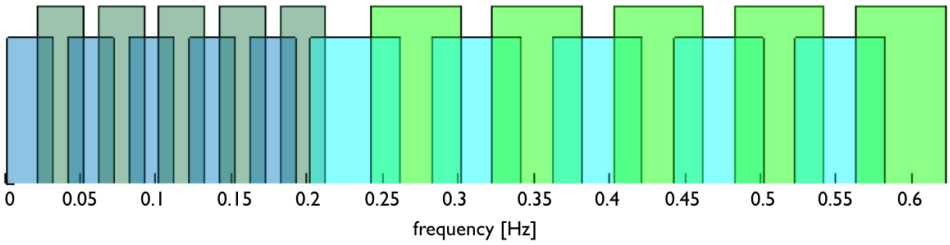

FIGURE 3.3: Frequency bands used to filter BOLD signal.

of voxels, that can be chosen in different ways. In our study we define nodes as the ROIs given by the atlas segmentation discussed before. Edges, the interconnections between nodes, can express structural, functional or effective connectivity. In graphs of functional networks, edges are weighted by the correlation coefficient R between the time series of two ROIs. Note that functional connectivity does not provide directionality or causality, so we worked with weighted undirected graphs. Having stated the premises, we obtained Correlation Matrices (CM) by calculating correlation coefficients R between TACs, having therefore a CM for each subject, each atlas, and each filtering band. However, to have this data representing a network some important steps are necessary (Bullmore and Sporns, 2009; Rubinov and Sporns, 2010). Generally speaking, a finite graph with N vertices can be represented with an $N \times N$ Adjacency Matrix (AM) (http://opendatastructures.org/versions/edition-0.1e/ods-java/12_1_AdjacencyMatrix_Repres.html), which has by definition, null entries in the main diagonal. So the first step was to subtract from Correlation Matrices their main diagonal. But the most crucial step is represented by thresholding, as we aim to include strong connections in our network. R values next to zero stand for poor connections, but the real question is how to set a threshold value θ in the $[0\ 1]$ interval to decide whether a connection is significant or not. It is important to remark that we took into account negative R values, that possibly represent strong relations, by considering the absolute value of our CMs. Also for networks to be the most comparable, we used a specific BCT function to normalize Correlation Matrices, to have weights in each of them cover the entire $[0\ 1]$ interval. To set a threshold several approaches have previously been considered (Rubinov and Sporns, 2010; Zuo et al., 2012; Achard and Bullmore, 2007) and recently compared (Welton et al., 2015); we implemented an hybrid method, that automatically chooses an optimal threshold θ_{opt} for each network to be constructed, it consists in maximizing Cost-Efficiency (C-E) of the resulting network. The reason to this, is that brain functional networks have been proven to have small-world characteristics (Sporns and Zwi, 2004; Latora and Marchiori, 2001), this topology is an attractive model

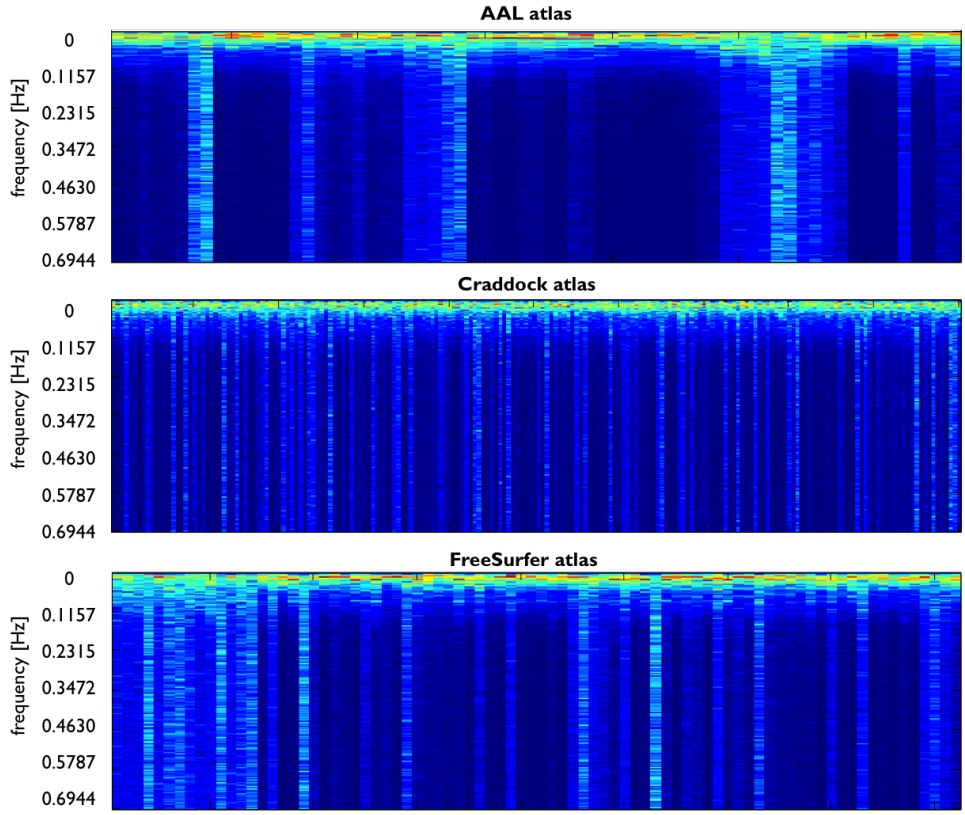

FIGURE 3.4: Power distribution across regions of interest for the three atlases. The dependence on frequency is displayed vertically, with low frequencies on the top and high frequencies on the bottom.

for brain network organization because it could support both segregated and distributed information processing, confer resilience against pathological attack, and minimise wiring costs (Achard and Bullmore, 2007). Also small-world networks are seen as systems that are both globally and locally efficient (Latora and Marchiori, 2001).

Since we are working with Weighted Undirected graphs, we defined network cost K as in (Ginestet et al., 2011), as the sum of all the elements of the Adjacency Matrix, divided by the possible number of edges:

$K = \frac{1}{N_V(N_V-1)} \sum_{i,j} a_{i,j}$

Then we evaluated Global Efficiency (E_G) using BCT (Rubinov and Sporns, 2010), and obtained Cost-Efficiency as $C\text{-}E = E_G - K$. This was computed for a grid of θ values, whose tightness has been decided a posteriori basing on the precision we wanted. To summarize, each AM was thresholded with a set of possible θ, and $C\text{-}E$ was calculated for each resulting network, making it possible to trace a $C\text{-}E(\theta)$ curve (example in Figure 3.5) and pick θ_{opt} as the value corresponding to the maximum of that curve. Eventually AMs were thresholded with their correspondent θ_{opt} and functional networks were ready for the subsequent measures on them.

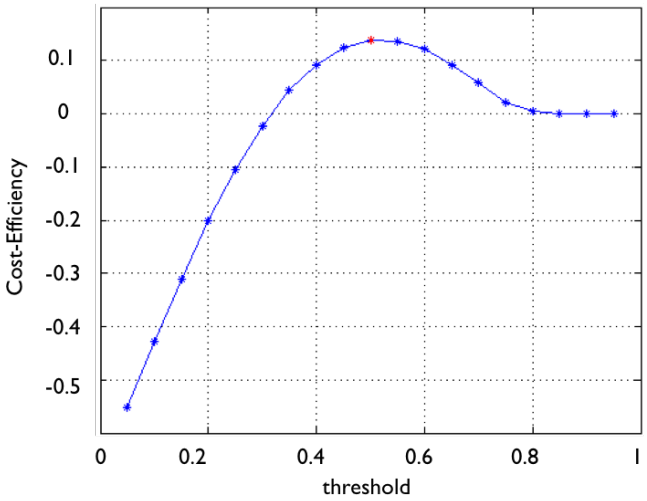

FIGURE 3.5: Example of C-$E(\theta)$ curve for a functional brain network.

3.3.2 dMRI

Individual brain networks were constructed basing on the set of reconstructed fiber tracts combined with the regions coming from the three different parcellation schemes. As van den Heuvel and Sporns suggest (Heuvel and Sporns, 2011), there are different ways to consider structural networks:

- Unweighted: if a streamline between region i and region j is present, the connection is included in the connectivity matrix, by setting the value of cell (i, j) to 1, and zero otherwise.

- Weighted by streamline count: this approach includes information on the quantity and/or efficacy of the existing connections. Information on the quantity of white matter connectivity between region i and region j is computed setting cell (i, j) of the AM to the sum of the existing streamlines that resulted from the fiber selection procedure.

- Weighted by streamline count, corrected for ROI volume: as volumes of the segmented regions are not uniform, the size of a ROI may influence the number of streamlines passing through it. Therefore, to control for this effect, the number of streamlines between region i and j can be normalized by the sum of the volumes of ROIs i and j. However this method is still controversial (Heuvel and Sporns, 2011) an we did not take it into account.

- Weighted by FA values: information on the integrity of the inter-regional white matter connections can be incorporated by estimating Fractional Anisotropy (FA) values for each of the interconnecting tracts. FA values express the level of anisotropic diffusion of white

matter in a brain voxel and are a commonly used metric to examine the microstructural aspects of brain connectivity.

We adopted the second method, and consistently with what we did with resting state data, we considered Weighted Undirected graphs for structural data too. The Adjacency Matrices we used for our analysis contain in cell (i, j) the number of fibres projecting from seed ROI i and to target ROI j (there is no direction, "seed" and "target" terms are used because typical of fiber tracking). If a track goes from ROI $i \rightarrow$ ROI $k \rightarrow$ ROI j, that counts only as a connection between i and j. We took individual networks and averaged them to obtain a single structural network, representative of our population. To avoid outliers we proceeded, as suggested in (Heuvel and Sporns, 2011), averaging an edge only if it was non-zero in at least 75% of the subjects, otherwise it was set to zero in the average AM. We then thresholded it to construct a network, we applied the same method discussed in the previous section to find an optimal threshold. There is though a difference between structural Adjacency Matrices built in the way specified above, and functional AMs. In fact values in the matrix to be thresholded are not uniformly distributed in the $[0\ 1]$ interval, as it is for functional data. This inhomogeneous distribution directly reflects in cost-efficiency curves, an example of this is visible in Figure 3.6, note the difference with 3.5. To compensate for this, we used an unequally spaced grid of possible thresholds, with values more concentrated near zero (see intervals between points in Figure 3.6).

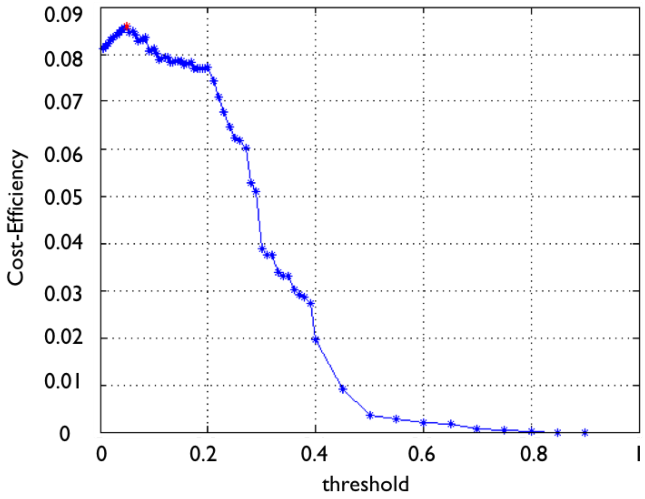

FIGURE 3.6: Example of C-$E(\theta)$ curve for a structural brain network.

3.4 Network Measures

With Adjacency Matrices representing networks, it was possible to apply BCT functions in order to obtain the desired network measures. Between all the metrics provided (https://sites.google.com/site/bctnet/measures/list) we focused on local measures that could provide information on the "hubbines" of our graphs. Centrality measures are the most straightforward way to highlight hubs, nodes that concentrate most of the connectivity. Six indices have been taken into account, but three were discarded as they gave poor results in terms of correlations and statistical significance. The three we present in the final results (Clustering Coefficient, Local Efficiency and Strength), are between those presented as the most reliable in a recent work (Welton et al., 2015), that aimed to assess reproducibility of graph-theoretic brain network metrics. What follows is a brief description of the indices we used, see Appendix A for their mathematical definition.

- **Betweenness Centrality**: the fraction of all shortest paths in the network that contain a given node. Nodes with high values of betweenness centrality participate in a large number of shortest paths.
- **Clustering Coefficient**: as a measure of functional segregation, it is based on the number of triangles in the network, with a high number of triangles implying segregation. Locally, the fraction of triangles around an individual node is known as the clustering coefficient and is equivalent to the fraction of the node's neighbours that are also neighbours of each other.
- **Local Efficiency**: a weighted path length is equal to the total sum of individual link lengths. Link lengths are inversely related to link weights, as large weights typically represent strong associations and close proximity. Local efficiency of a particular vertex is the inverse of the average shortest path connecting all neighbours of that vertex.
- **Strength**: the degree of an individual node is equal to the number of links connected to that node, Individual values of the degree therefore reflect importance of nodes in the network. Strength is the weighted variant of the degree, and is defined as the sum of all neighbouring link weights.
- **Participation Coefficient**: assesses the diversity of intermodular interconnections of individual nodes, comparing the number of links (order, degree) of node i to nodes in all clusters with its number of links within its own cluster.

- **Within-module Degree**: it is the within-module version of degree centrality. This measure requires determining a community structure. The optimal community structure is a subdivision of the network into nonoverlapping groups of nodes in a way that maximizes the number of within-group edges, and minimizes the number of between-group edges.

We want to show, using these indices, that nodes showing hub behaviour are also those who are potentially more plastic. Hubs have already been shown to correspond to brain regions that exhibit complex physiological responses and maintain widespread and diverse connection profiles with other parts of the brain (Sporns and Heuvel, 2013). For R-fMRI data, we computed the measures above for each individual network, so each one of the 20 subjects had its own set of graph-theoretical measures. For the subsequent step - assessing the relationship with PET measures - population indexes were needed, so we averaged across subjects. This is a substantial difference from what we did with DTI data, where we averaged Adjacency Matrices across subjects (Figure 3.7). However we also tried implementing the "average matrix" method even for R-fMRI data, a comparison between the two methods can be found in the Discussion chapter, section 5.2.2.

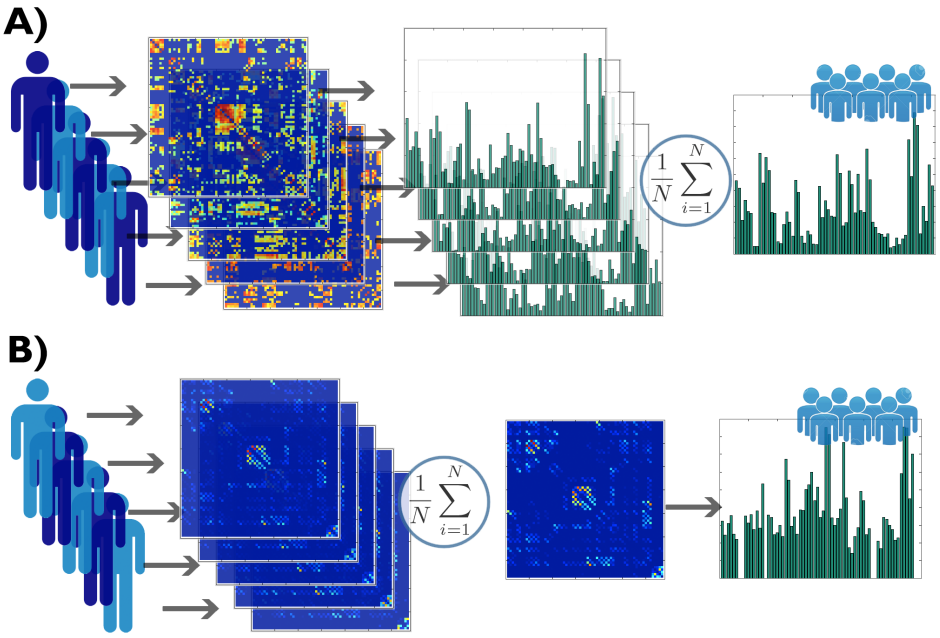

FIGURE 3.7: Different ways to obtain population network measures: A) R-fMRI data processing pipeline, B) dMRI data processing pipeline.

3.5 Correlations

We evaluated Pearson correlation coefficient between PET measures across ROIs and the various network measures across the same ROIs. We obtained therefore a couple of values $[R, p]$ for each atlas, PET measure, network index and filtering band. A significance threshold for p-values was set to 5%. Correlations were evaluated also between functional and structural network measures, and between PET and structural network measures. As introduced before, our main aim was to assess the correlation between measures of functional connectivity and cerebral protein synthesis, focusing on the part that cannot be explained by metabolic rate, and therefore belongs to other on-going processes. To do so we calculated partial correlations, using FDG PET as a confounding factor. FDG though was not the only covariate we used to assess correlations between R-fMRI and rCPS, and we considered other variables that could possibly affect results:

- ROIs dimension: the number of voxels making up a region.
- Power distribution across regions: when we bandpass filtered each TAC, we took note of their power spectrum, and the fraction of it determined by each filtering band. Doing this, for a fixed band, ROIs would have different amount of power between them, with respect to the total TAC. A representation of it can be found in Figure 3.4 in the Temporal Filtering section.

Again, *p-values* were taken into account to set to zero the correlations that did not match the 5% threshold requirement.

3.6 Sliding Windows

We tried to focus on hubs stability over the time, using a different approach from the frequency analysis described up to now. We used sliding windows of various lengths to take into account part of the original TAC, which was made up by 1200 samples (see Datasets section, 2.1.1). Each window was built to overlap the previous one by 80% of its width, and in this way sweep through all the samples of the original TAC and construct a network for each windowed TAC portion (see Figure 3.8). Doing so, we aimed to find out if rhythmical processes were present through the 15 minutes R-fMRI scans. Variability was evaluated calculating network measures' standard deviations across the sliding window. This standard deviation was divided by its mean, obtaining a coefficient of variation (CV), which was then averaged between subjects. Eventually, population CV was correlated against PET measures: FDG, rCPS and rCPS using FDG and ROIs dimension as covariates.

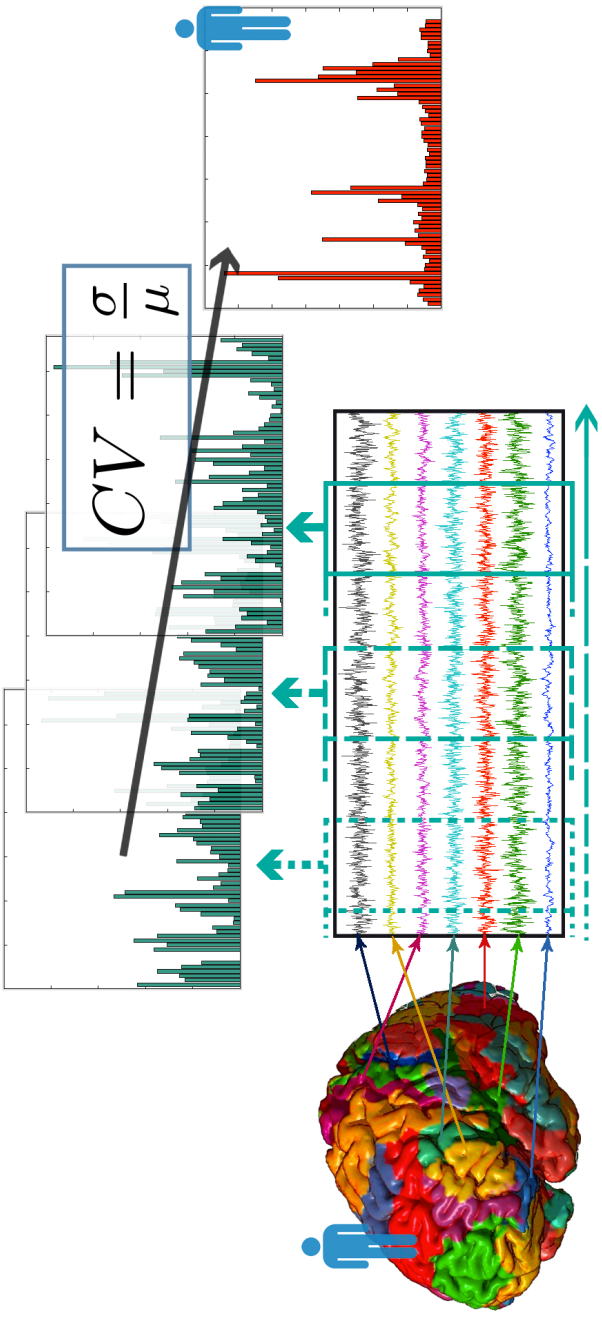

FIGURE 3.8: overview of the Sliding Windows analysis.

Chapter 4

Results

4.1 R-fMRI vs. dMRI

The relationship between structural and functional connectivity is a topic of great interest for the contemporary neurosciences; the evidence so fat suggests that structural connectivity places constraints on which functional interactions occur in the brain network (Sporns, Tononi, and Edelman, 2000). By means of those constraints, structure can predict function by shaping neural dynamics among cells and brain region (Honey, Thivierge, and Sporns, 2010). Specifically, the average statistical dependencies of the BOLD signal between two nodes over low frequencies (5 to 10 minutes) reflects the underlying structural connectivity determined with DTI (Park and Friston, 2013). Skudlarski et al. first assessed the relationship between Diffusion Tensor Imaging and Resting State Temporal Correlations (Skudlarski et al., 2008). They demonstrated strong association between the brain connectivity matrices obtained from the two different imaging techniques. The association was very high for strongly connected regions and weaker, but still statistically significant for most other region pairs.

On the premises above, we expected significant correlations between network measures obtained from structural and functional networks, possibly higher at lower frequencies.

As showed in Figure 4.1 and reported in Table 4.1a, we found that correlations were statistically significant and high, in particular for AAL and FreeSurfer atlases R values are between 0.3 and 0.7, with $p\text{-}values<0.002$. The lower values found with the Craddock atlas could be explained by its segmentation into functional coherent regions without a solid description of white matter (WM) where the fMRI signal is relatively scarce (Gawryluk, Mazerolle, and D'Arcy, 2014). Both the results for the AAL and FreeSurfer segmentations suggest weak linear trends across frequency bands that increase in the lower frequency range.

	Clustering Coefficient	Local Efficiency	Strength
a)	**R-fMRI vs. DTI**		
	AAL	$0.29 \div 0.46\,, p < 0.019$	$0.52 \div 0.64\,, p < 0.001$	$0.49 \div 0.76\,, p < 0.001$
	Craddock	$0.19 \div 0.34\,, p < 0.008$	$0.34 \div 0.50\,, p < 0.001$	$0.31 \div 0.45\,, p < 0.001$
	FreeSurfer	$0.35 \div 0.49\,, p < 0.002$	$0.62 \div 0.72\,, p < 0.001$	$0.53 \div 0.64\,, p < 0.001$
b)	**R-fMRI vs. FDG Standardized Uptake Value**		
	AAL	$0.22 \div 0.36\,, p < 0.042$	$0.21 \div 0.36\,, p < 0.037$	$0.19 \div 0.38\,, p < 0.025$
	Craddock	$0.28 \div 0.62\,, p < 0.001$	$0.53 \div 0.67\,, p < 0.001$	$0.42 \div 0.64\,, p < 0.001$
	FreeSurfer	$0.46 \div 0.59\,, p < 0.001$	$0.43 \div 0.60\,, p < 0.001$	$0.27 \div 0.49\,, p < 0.015$
c)	**R-fMRI vs. regional Cerebral Protein Synthesis**		
	AAL	$0.59 \div 0.69\,, p < 0.001$	$0.58 \div 0.68\,, p < 0.001$	$0.48 \div 0.65\,, p < 0.001$
	Craddock	$0.40 \div 0.68\,, p < 0.001$	$0.55 \div 0.69\,, p < 0.001$	$0.44 \div 0.60\,, p < 0.001$
	FreeSurfer	$0.67 \div 0.81\,, p < 0.001$	$0.66 \div 0.81\,, p < 0.001$	$0.51 \div 0.68\,, p < 0.001$
d)	**R-fMRI vs. rCPS, controlling for FDG, ROIs dimension, power distribution**		
	AAL	$0.39 \div 0.63\,, p < 0.002$	$0.39 \div 0.63\,, p < 0.002$	$0.26 \div 0.57\,, p < 0.037$
	Craddock	$0.22 \div 0.45\,, p < 0.002$	$0.19 \div 0.44\,, p < 0.009$	$0.15 \div 0.33\,, p < 0.030$
	FreeSurfer	$0.39 \div 0.69\,, p < 0.001$	$0.41 \div 0.71\,, p < 0.001$	$0.37 \div 0.61\,, p < 0.001$

TABLE 4.1: ranges for R values of the various relationships investigated

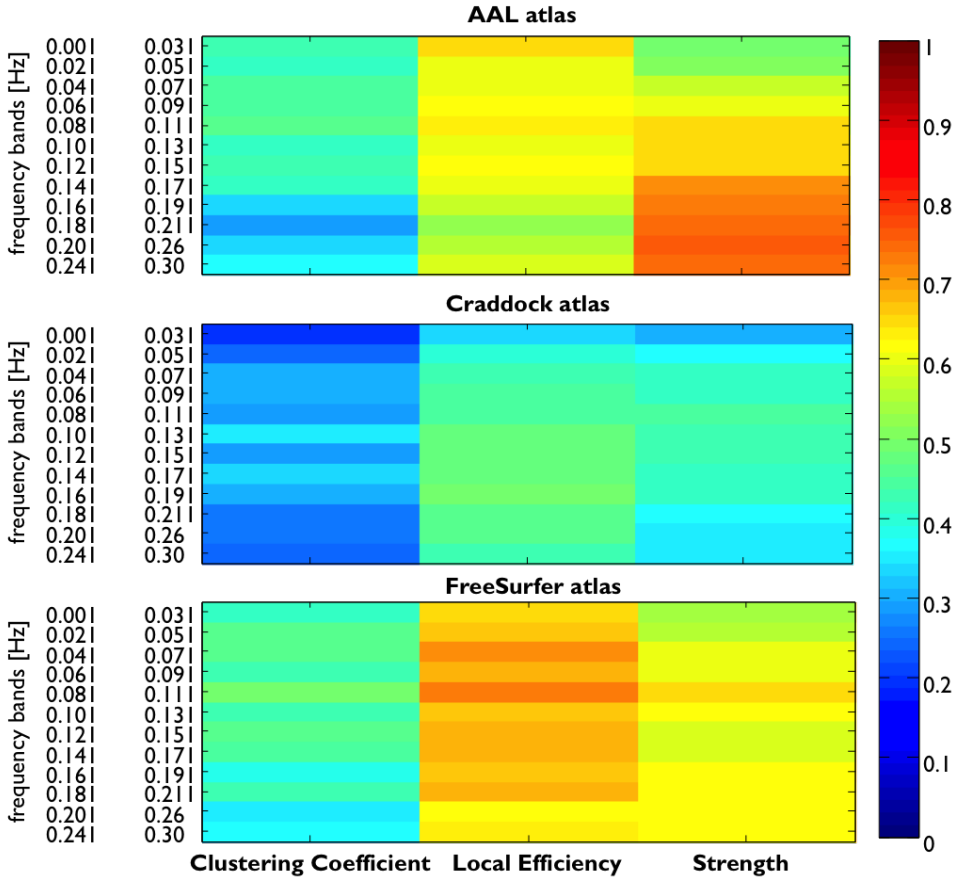

FIGURE 4.1: Correlations (R values) between functional and structural network measures (Clustering Coefficient, Local Efficiency and Strength). The dependence on the R-fMRI filtering band is shown. Results are reported for the three different parcellation schemes.

4.2 PET measures

Here we studied how protein synthesis in the cortex and glucose consumption are related phenomena. We used [^{18}F]FDG as a proxy measure of node synaptic activity as more than 85% of cerebral glucose is used by neurons and mainly by presynaptic axon terminals. To evaluate the relationship between rCPS and metabolic rate, we calculated Pearson correlation between [^{18}F]FDG and L-[1-^{11}C]Leucine data.

The scatter plots are presented in Figure 4.2, correlations are $R_{AAL} = 0.537$, $R_{CR} = 0.620$, $R_{FS} = 0.628$, *p-values* are $< 10^{-5}$. This implies the existence of a strong relationship between the two measures; we took this into account when assessing correlations between PET Leucine and R-fMRI-derived network measures.

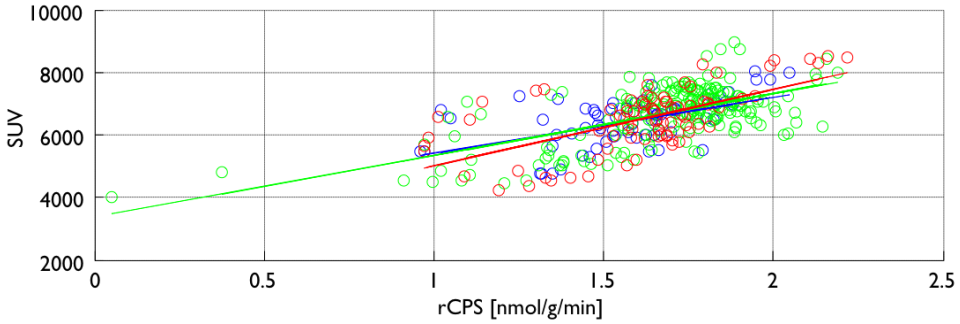

FIGURE 4.2: Scatter plot of L-[1-^{11}C]Leucine and [^{18}F]FDG data, the three colours stand for the three atlases (blue for Automated Anatomical Labeling, green for Craddock and red for FreeSurfer), straight lines represent the linear regressions.

4.3 R-fMRI vs. PET

4.3.1 [^{18}F]FDG

The relationship between functional connectivity and glucose consumption is far from being completely understood, but many recent studies investigated this relationship, analysing data coming from PET FDG and resting state fMRI scans. Glucose, brain's main energy source, is consumed 30% for basal metabolism (in the absence of connectivity), suggesting that the spontaneous brain activity takes 70% of the energy consumed by the brain. This large portion reflects intrinsic activity of uncertain functional origin, and for this reason it is sometimes referred to as "dark energy" (Tomasi, Wang, and Volkow, 2013). It has been demonstrated though a significant interaction between local neuronal activity (measured with [^{18}F]FDG) and the generation of Functional Connectivity from BOLD fMRI data (Riedl et al., 2014). This interaction has been recently studied (Aiello et al., 2015), showing that the relative glucose uptake, assessed by FDG PET, and metrics of functional connectivity derived from R-fMRI are significantly correlated.
With this background, we were expecting what results confirmed (Figure 4.3): a positive correlation between network indices of centrality and FDG SUV. In fact we have for Craddock and FreeSurfer atlases Pearson correlations between 0.27 and 0.67, with *p-values* always below 10^{-3} (except for Strength in FreeSurfer where $p < 0.015$). In other words we can say that nodes showing greater centrality, tend to have higher metabolic rate. Metabolism in brain is most intense in the cortical areas, this could be a reason AAL atlas, with its loose cortical parcellation, exhibits poor correlations between FDG SUV and functional network measures. The remaining atlases show a stronger correlation. Detailed values in Table 4.1b.

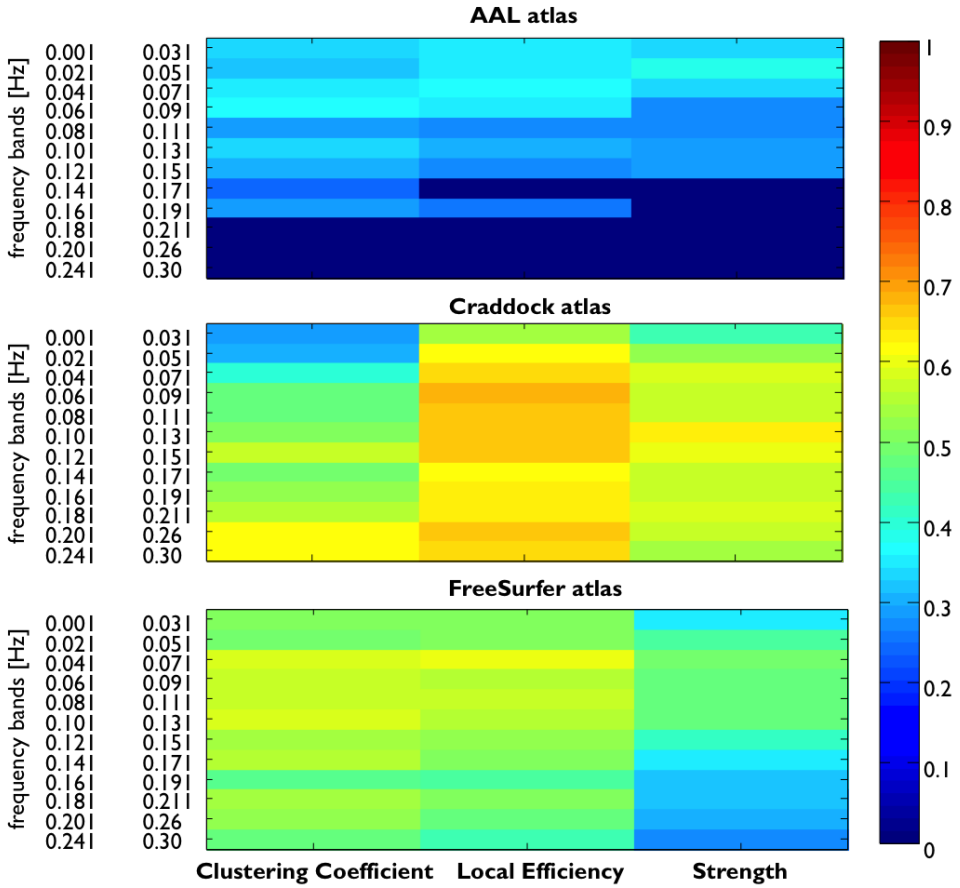

FIGURE 4.3: Correlations between functional network measures and [^{18}F]FDG PET. Results are reported for the three atlases, and the dependence on the filtering band is shown.

4.3.2 L-[1-^{11}C]Leucine

A positive correlation between functional network indices and rCPS measured with L-[1-^{11}C]Leucine PET, stands for intense protein synthesis in functional hubs, adding information on the metabolism in hubs discussed above.

As we show in Figure 4.4, functional network measures appear to be strongly related to the rate of Cerebral Protein Synthesis, especially for the third atlas, where R values span between 0.51 and 0.81, with $p < 10^{-3}$. For the remaining atlases, correlations are statistically significant as well, as visible in Table 4.1c. Even if trends seem to emerge (Clustering Coefficient in the Craddock atlas, and all the measures in FreeSurfer atlas), we did not evaluate them at this stage of the analysis.

As stated before, some corrections are needed, in order to consider the portion of Functional Connectivity – rCPS relationship that cannot be explained by metabolism. Introducing the three covariates listed in section (3.5) (FDG SUV, ROI dimension and power distribution), we calculated

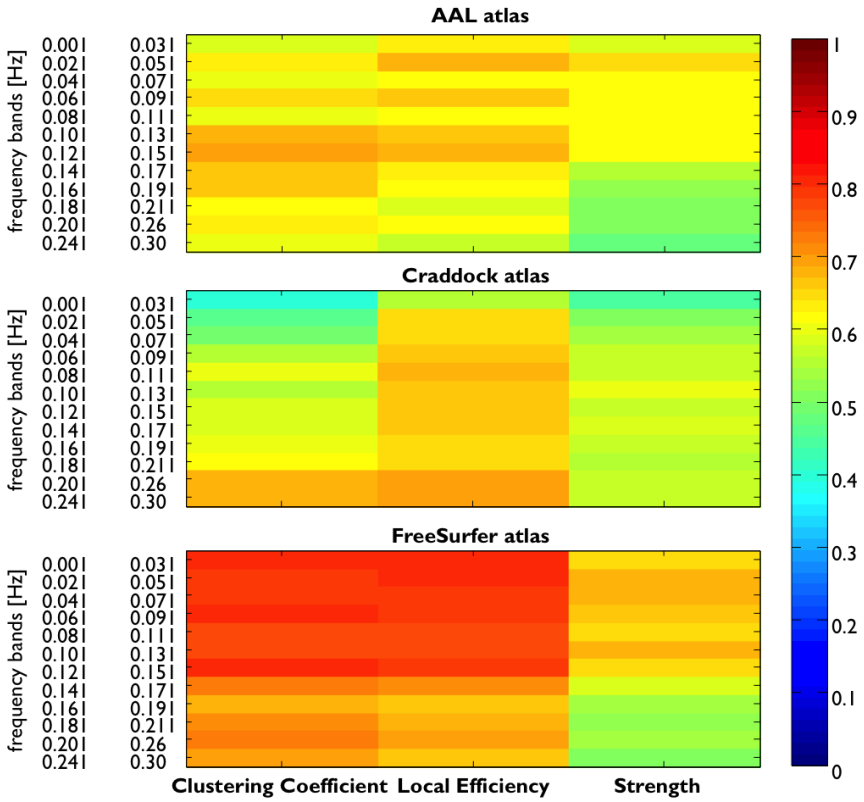

FIGURE 4.4: Correlations between functional network measures and Leucine PET. Results are reported for the three atlases, and the dependence on the filtering band is shown.

correlations, presented in Figure 4.5, standing for the relationship between rCPS and network measures that cannot be explained by metabolic rate. Ranges and p-values are in Table 4.1d. Correlations remain quite strong,

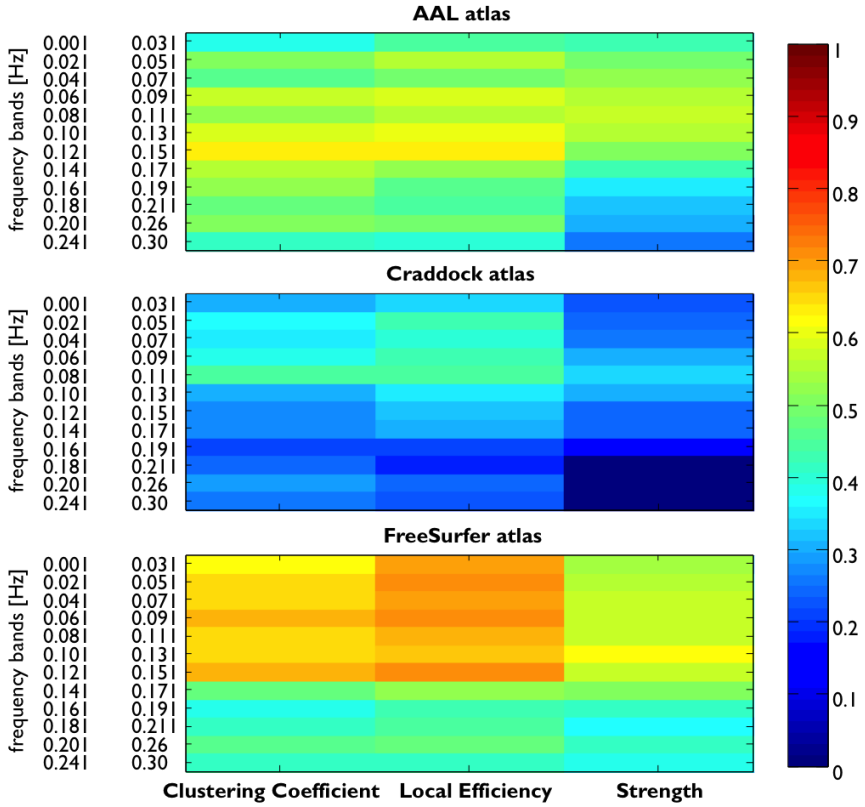

FIGURE 4.5: Partial correlations between functional network measures and Leucine PET, using as covariates: FDG PET, ROIs dimension and power distribution across ROIs. Results are reported for the three atlases, and the dependence on the filtering band is shown.

and also coherence across the atlases is present, this enforces results, suggesting they are not critically dependent on the particular parcellation scheme used. In Figure 4.5 some trends are appearing, suggesting the presence of a "preferred" frequency band, where correlations are stronger. In Figure 4.6 are showed the same data of Figure 4.5, in a way that trends are more visible. We fitted these data with 3rd degree polynomial curves, implementing the Tukey bisquare estimator for robust fitting. Weights were given by $1-p$ relatively to each R value. Correlations across frequency bands appear to be well fitted by 3$^{\text{rd}}$ degree polynomials. Coefficients of determination (R^2) for the fits are: AAL atlas: 0.73, 0.66, 0.96, Craddock atlas: 0.74, 0.92, 0.87, FreeSurfer atlas: 0.82, 0.89, 0.86, for Clustering Coefficient, Local Efficiency and Strength respectively. Other details on the goodness of the fit can be found in Appendix A.

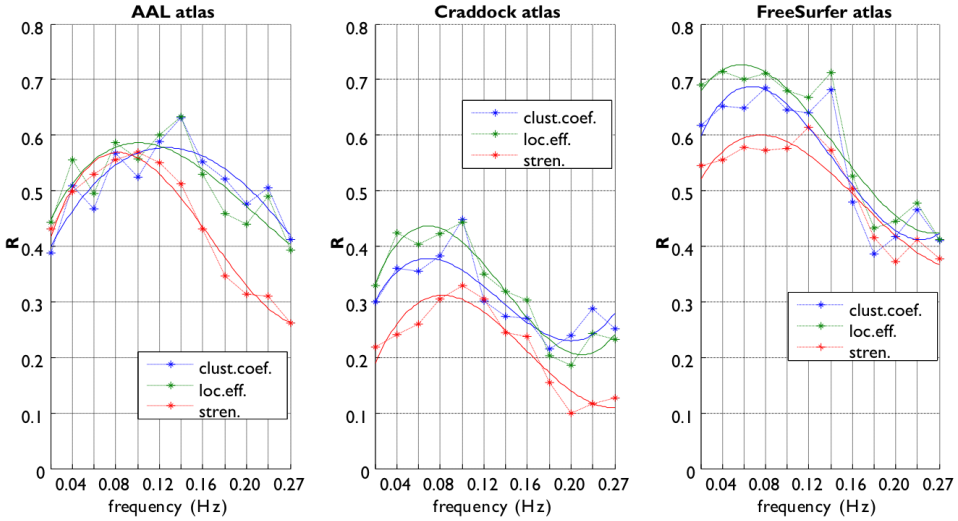

FIGURE 4.6: Correlations between R-fMRI network measures and rate of cerebral protein synthesis, as function of BOLD signal frequency, considering as covariates FDG PET, ROIs dimension and power distribution. Solid lines represent the 3rd degree polynomial interpolation of data points.

4.4 dMRI vs. PET

Correlating structural network measures with PET data gives poor information. Many *R* values are not statistically significant with a threshold level set to 5%, and no consistence across atlases or measures is found. When it comes to structural data, the atlases show substantial differences, as white matter is barely taken into account in FreeSurfer atlas, and the rationale Craddock atlas is based upon, is given by functional MRI. Taking into account this, together with what already said about PET data, can explain why a comparison between PET measures, and structural network indices gives no interesting information.

4.5 Sliding Windows

Results show a strong negative correlation between PET and CV of network indices. We can assume that metabolism and protein synthesis tend to be greater in regions that exhibit stable indices of centrality during the time. Since network hubs are highlighted in resting state, they must be responsible for the background activity of the brain. These basic routines have to be necessarily active most of the time, and on these premises our results enforce the idea that regions showing stable indices of centrality are the most active in terms of metabolism and protein synthesis. Missing data in the AAL atlas stand for "Not a Number" values, that emerge when computing

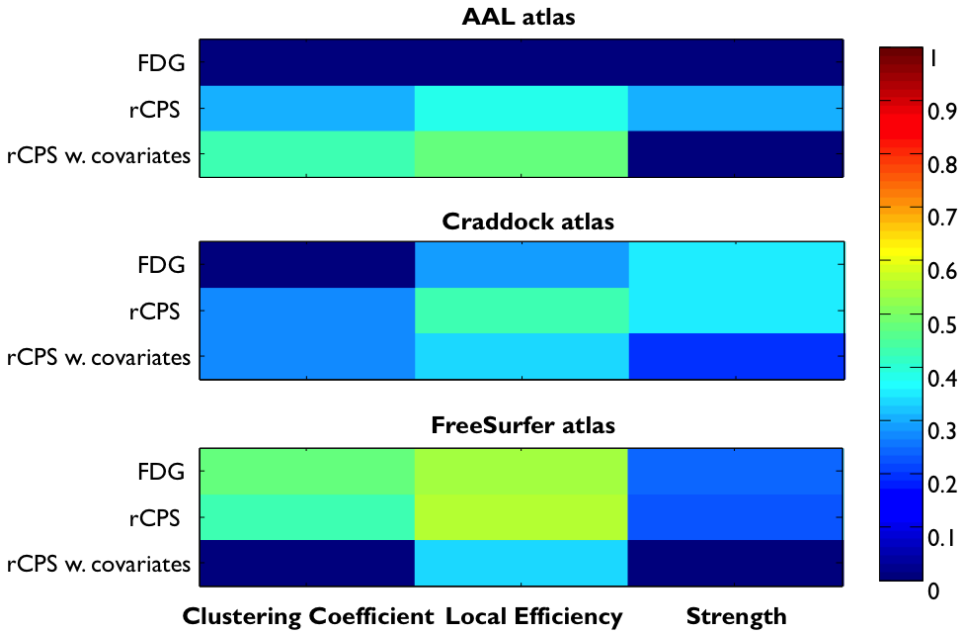

FIGURE 4.7: Correlations between DTI-derived network measures and PET measures. Results are reported for the three atlases, rows labelled as "rCPS w. covariates" report partial correlations between the network measures and L-[1-^{11}C]Leucine, accounting for FDG metabolism and ROI dimension.

a CV and the denominator is equal to zero. This happens for broad windows (750 and 500 samples), because few of them are needed to cover the whole TAC, so mean and standard deviation are computed between few values.

4.6 [^{11}C]PiB PET

We introduced in this study a third PET tracer, Pittsburgh compound B, mainly used to highlight beta-amyloid plaques in neuronal tissue, and therefore important in Alzheimer's Disease Research (Klunk et al., 2004). In the present work, we used a distribution volume ratio (DVR) template, which provides information on myelin density. The purpose of doing this, was to check if the rCPS-fMRI relationship was influenced by myelin density, expecting though a negative answer. That is because there is no basis to suppose that myelin, covering axons and therefore well present in white matter, has a strong correlation with fMRI and functional connectivity, involving mostly grey matter.

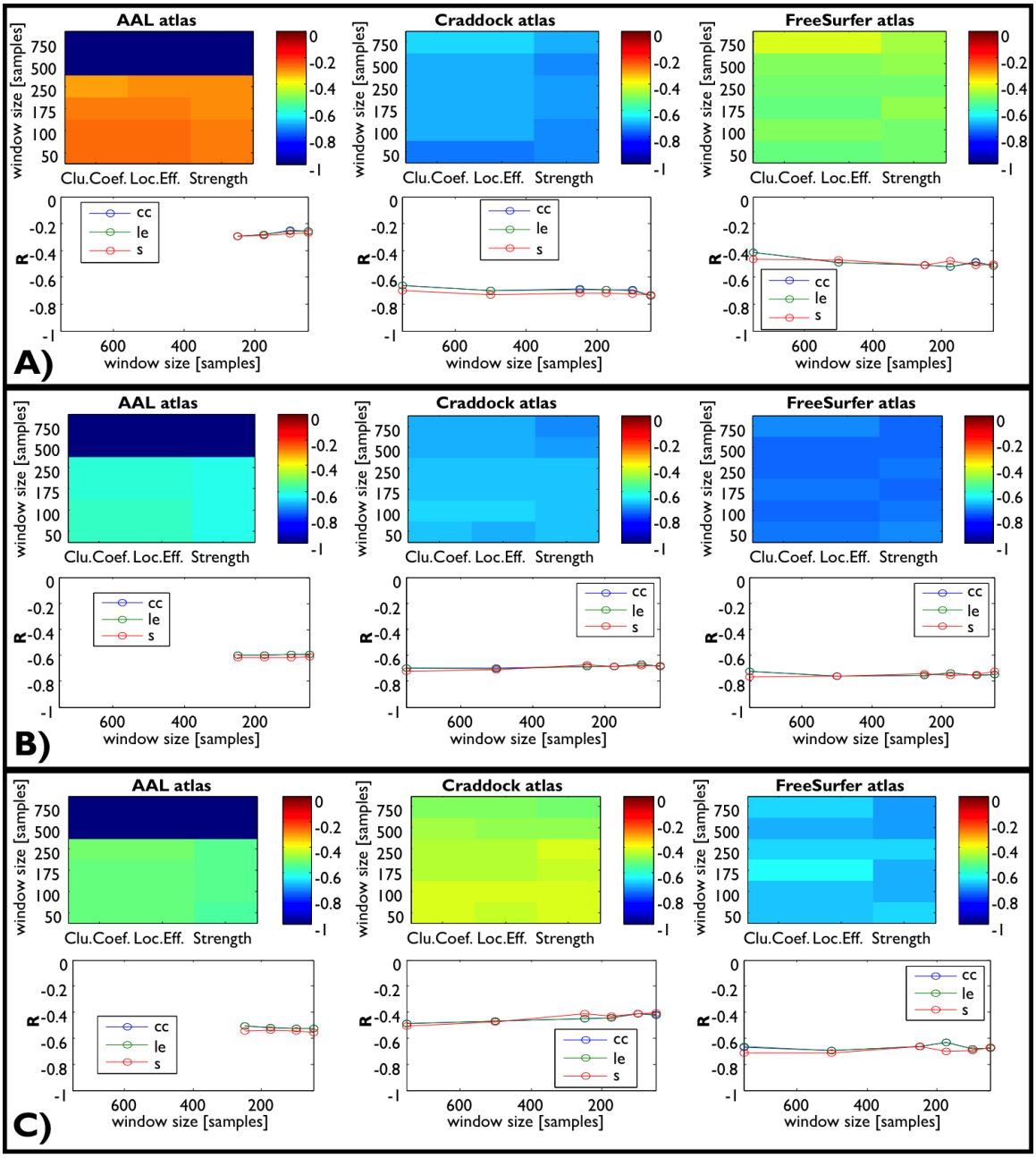

FIGURE 4.8: Correlations between functional network measures' *CV* and PET measures. The bottom three images in each of the frames report the same results as the top ones, but shown in a different way to highlight possible trends. The dependency on the sliding window size is shown. The three frames report results for: A) FDG PET – B) Leucine PET – C) Leucine PET, using as covariates FDG and ROIs dimension.

4.6.1 Acquisition

Data came from a study (Veronese et al., 2015) that involved 10 volunteer healthy subjects: 3 male and 7 female, age: 29.5±6.2 years. Each of them was scanned twice, with the retest scan performed within approximately 1 month from the baseline. Exams were performed on the high resolution research tomograph (HRRT) (CPS Innovations, Knoxville, TN, USA), a brain dedicated PET scanner (Wienhard et al., 2002).
Scans lasted 90 minutes, beginning with a 1-minute intravenous bolus injection of [^{11}C]PiB (mean 358±34 MBq). Images were reconstructed using the 3D ordinary Poisson ordered subset expectation maximization algorithm (POSEM). All the resulting dynamic PET images consisted of 25 frames of data with a voxel size of 1.22mm×1.22mm×1.22mm. Interframe subject motion correction was applied by realigning each PET frame to a common reference space. The first six frames of each scan corresponding to the first 6 minutes of acquisition were moved together because of the lack of spatial information necessary for the image coregistration. The procedure was applied to each PET study and all the reconstructed images but no frame or subject were discarded for exceed of motion. Data were also corrected for carbon-11 decay. In addition to the PET scans, all subjects underwent a 3D anatomic brain magnetic resonance imaging (MRI) using a 3T Siemens system (Siemens, Erlangen, Germany; TRIO 32-channel TIM system): T1-weighted MPRAGE (echo time/inversion time/repetition time = 2.9/900/2,300, flip angle = 8°, pixel resolution = 1×1×1.1 mm). Grey matter, white matter, and basal ganglia were automatically extracted from MRI image by combining outputs from VBM8 toolbox (`http://dbm.neuro.uni-jena.de/vbm/download/`) and FIRST (`http://fsl.fmrib.ox.ac.uk/fsl/`) using a probability threshold of 90%. Segmented MRI images were hence coregistered to PET using rigid transformation estimated using Flirt (`http://fsl.fmrib.ox.ac.uk/fsl/`) maintaining PET data in its original space and avoiding further loss of resolution due to interpolation.

4.6.2 Quantification

Detailed information can be found in the original article (Veronese et al., 2015). Quantification of PiB PET images followed reference region approaches. In general, a reference region method consists of a two-step procedure that requires: the selection of a brain tissue region containing no or negligible amount of specific binding and the use of a quantification model in which the plasma tracer information can be replaced with the tracer activity in the reference region. For the extraction of the reference time-activity curve (TAC), authors of (Veronese et al., 2015) used the supervised clustering

method developed by Turkheimer et al. (http://jnm.snmjournals.org/content/48/1/158) and already validated for [^{11}C]PiB PET tracer by Ikoma et al. (doi: 10.1038/jcbfm.2013.133). This method consists of the multiple regression of all PET image voxel TACs on a predefined set of kinetic classes. After regression, all the voxels associated to the reference class with probability >90% are combined together and the average of their TACs defines the reference input function. Once the reference TAC was extracted, [^{11}C]PiB binding was calculated by application of a kinetic operator to the measured dynamic PET activity. Distribution volume ratio (DVR) is the parameter of interest because it is directly linked to tracer-target affinity as well as the target density. In the instance here, in which [^{11}C]PiB is used as a myelin marker, the DVR becomes a proxy of myelin density. For the Logan analysis, authors chose to apply both the standard Logan with reference (Logan) and the Logan with reference corrected for k2 value (Logan_k2). The latter has showed to recover part of the bias that affects Logan approaches when applied at the voxel level. The literature was followed to define the settings ($k_2 = 0.149\ min^{-1}$), while for both Logan and Logan_k2 the last 60 minutes of the experiment were used for the DVR calculation. The Logan approach with k2 correction produced comparable estimates with the standard Logan approach with the reference region: the means of voxel estimates within ROIs were almost identical. The WM-GM contrast measured by the Logan modified approach was identical to the one measured with the standard approach both in amplitude and in variability. Given the reported strong similarity between the two measures, Logan with k2 correction was omitted from subsequent analyses. Therefore standard Logan was used to create from the 10 subjects a [^{11}C]PiB DVR template in stereotaxic MNI space, that we used in the present research.

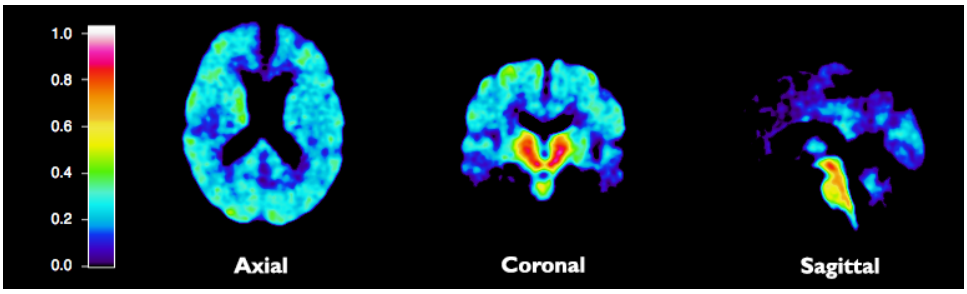

FIGURE 4.9: [^{11}C]PiB DVR template

4.6.3 [^{11}C]PiB results

As we can see in Figure 4.10, there is no substantial relationship between myelin density and regional cerebral protein synthesis, matching what our expectations were, correlations are poor and not statistically significant.

This proves that myelin density is not a factor we must consider when assessing the relation between functional connectivity and cerebral protein synthesis. It should be interesting though to study those interactions in case of neurodegenerative diseases.

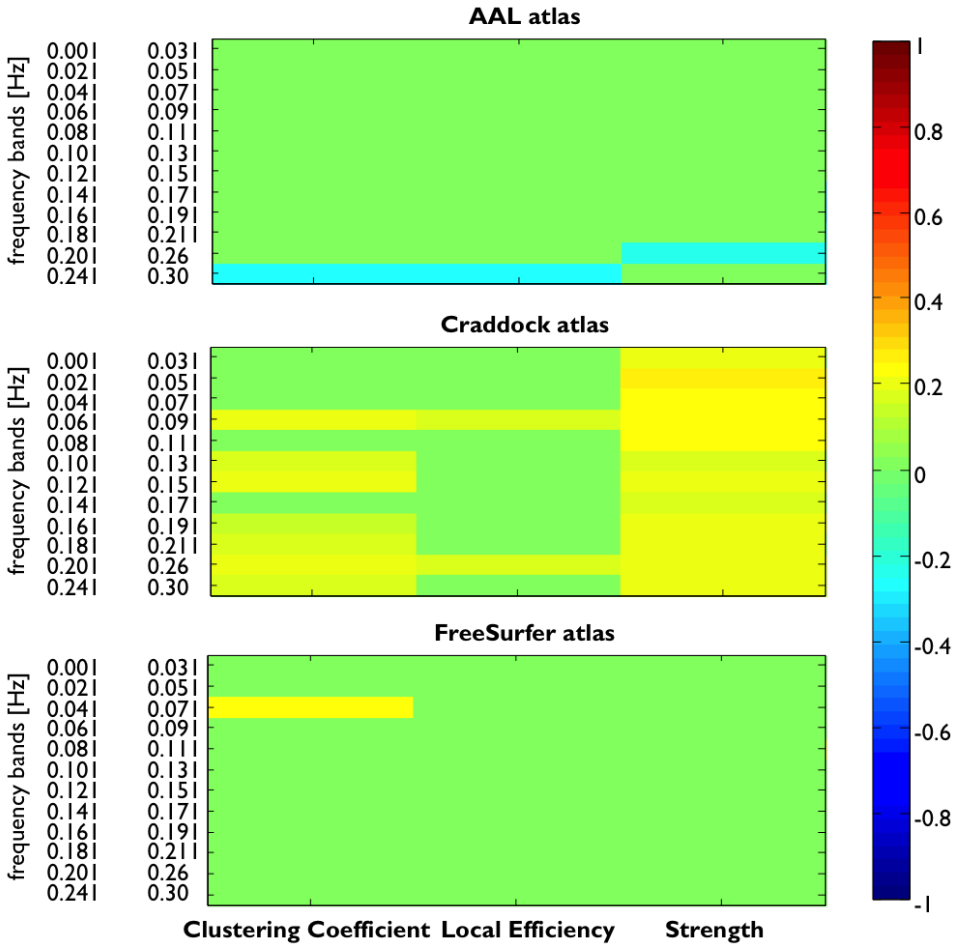

FIGURE 4.10: Correlations between functional network measures and PiB PET, results and their dependence on the filtering band are presented for the three atlases. Values identical to zero are not statistically significant, with a 5% threshold for p-values.

Chapter 5

Discussion

5.1 Main Findings

Using a graph theoretical approach, we demonstrated that a strong relationship exists between functional connectivity and the rate of cerebral protein synthesis. This relationship remains even when we consider metabolism as a confounding factor, implying that network hubs are generally the ones that exhibit greater protein synthesis not linked to energetic demands. This relationship is driven by the time scale taken into exam, with correlations higher for BOLD frequencies between 0.06 and 0.12 Hz, and decreasing at higher frequencies.
With results coming from the sliding windows approach, we could also demonstrate that protein synthesis, hubbiness and stability over the time are linked concepts, since regions showing more stable *hub* properties tend to have greater protein turnover.
Results are consistent across the different parcellation schemes used, differences can be explained as they do not exhibit contradictions with the *rationale* behind the different segmentations. However for this particular kind of studies FreeSurfer atlas seems to be the most suitable, as it offers a more precise description of the cortex.
Theoretical network measures, as stated before, do not provide a straightforward biological interpretation. Nonetheless when such measures are compared to objective biological quantities, coherence emerges between the two. This can in some way validate the graph theoretical approach as a methodology to study the connectivity of human brain.

5.2 Limitations

5.2.1 Graph threshold

As discussed in the Network Construction chapter, different approaches have been utilised in literature to set a threshold to graphs, the most common was to do it at a range of sparsities. Other approaches consisted in a

fixed threshold, mean degree thresholding, and others presented in (Welton et al., 2015). One study (Guo et al., 2012) compared the use of a fixed threshold with soft and proportional thresholding techniques, but found neither to be significantly more reliable.

Hence our maximum Cost-Efficiency method could be a valid alternative to the ones stated above. We performed a comparison between results obtained with our method, and the ones obtained fixing three different sparsity levels, chosen to span in the cost interval that typically characterises small-world regime (Achard and Bullmore, 2007). Results, presented in figure 5.1, suggest contemporarily that our main findings are strong, and that the maximum Cost-Efficiency method to threshold networks is reliable. Results suggest that as long as a threshold guarantees the small-world

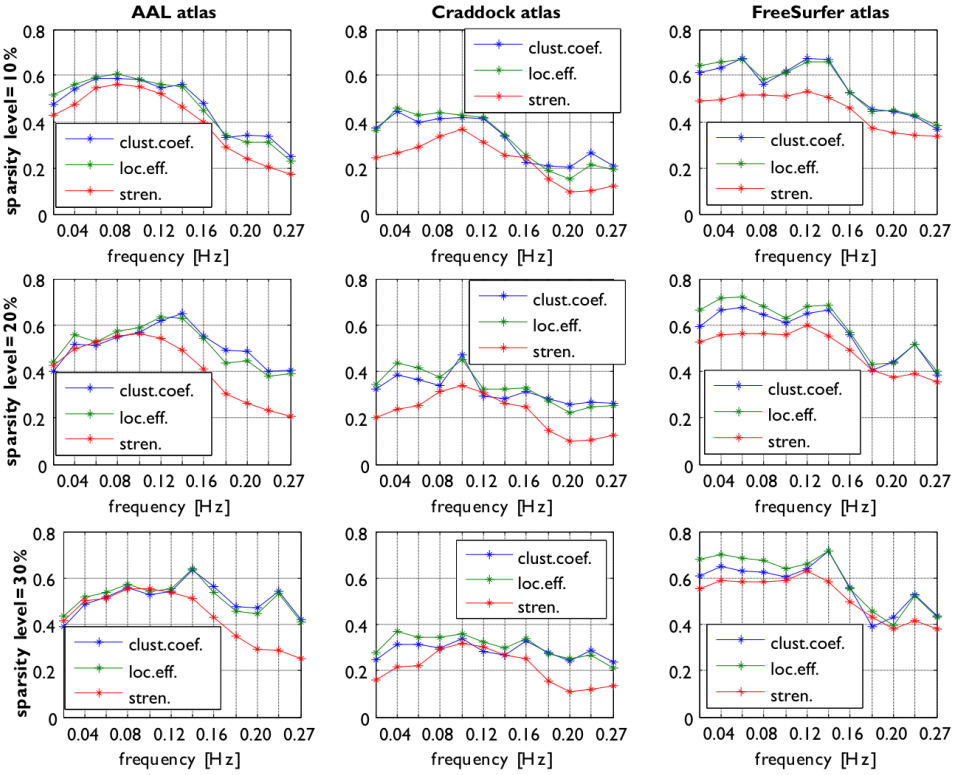

FIGURE 5.1: Correlations between functional network measures and rCPS, controlling for FDG, ROI dimension and power distribution. Results refer to the different atlases (horizontally) and the three sparsity levels used to construct networks.

regime, its choice is not critical. We recommend though to consider sparsity levels over absolute thresholds, as the first ones directly reflect information about cost of resulting networks. These findings point in the same direction of a recent work (Borchardt et al., 2016), showing that when networks are thresholded with a sparsity level between 16% and 22% (a subinterval of the one we tested), the biggest differences emerge from the comparison

between brain networks coming from healthy controls and patients with major depression.

5.2.2 Average network measures vs. average correlation matrices

As showed in Figure 3.7 and explained in section 3.4, we followed two different approaches to obtain population network indices from resting state and structural MR data. What we did for R-fMRI data is probably the most straightforward way to obtain population metrics. In the meanwhile, averaging correlation matrices – what we did for dMRI – was validated in literature (Heuvel and Sporns, 2011).
We implemented the "average correlation matrix" method for resting state data, in order to assess how much results would change adopting one method rather than the other. First of all, as in Figure 5.2, we can say that network

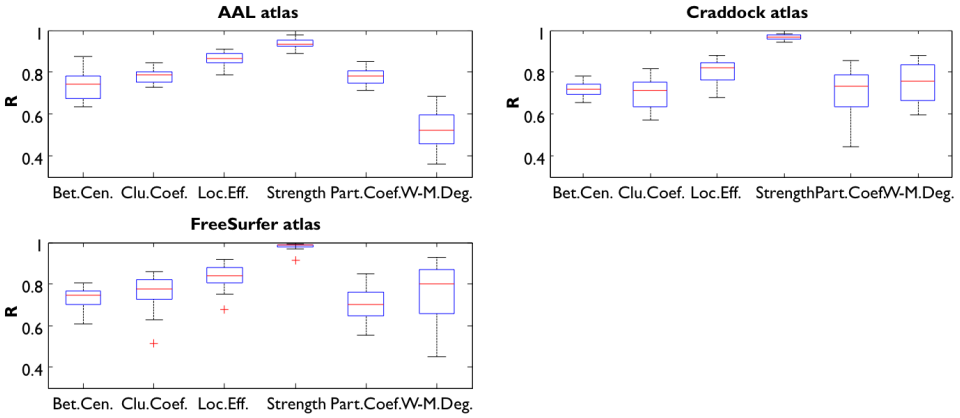

FIGURE 5.2: Correlations between population indices obtained with the two methods presented in section 3.4: averaging network measures and averaging correlation matrices

measures are strongly related between the two methods, and this is a first hint telling that differences in results are not drastic. We can also see those R values in figure to represent some sort of reproducibility of theoretical network measures themselves, as they tend to be not critically dependent on the preprocessing scheme adopted. These findings seem to point in the same direction of the already cited work by Welton et al. (Welton et al., 2015), and they confirm the choice we previously did, to focus on Clustering Coefficient, Local Efficiency and Strength measures, discarding the other measures.
Correlating PET data against functional network measures, obtained with the "average correlation matrix" method, gives the results reported in Figure 5.3. Comparing this with our main findings in the Results chapter (Fig-

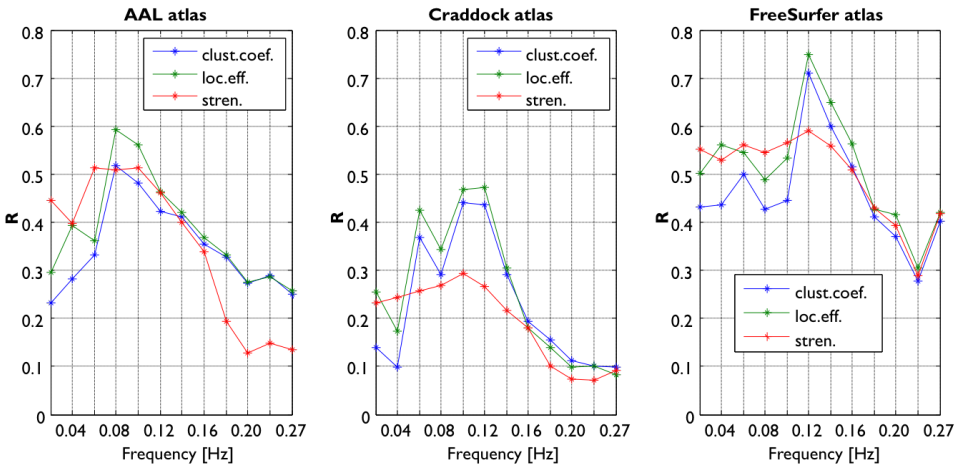

FIGURE 5.3: Average correlation matrix method, partial R values between R-fMRI-derived network measures and rCPS, controlling for FDG, ROI dimension and power distribution. Asterisks stand for actual data points, lines are their linear interpolation. Results are reported for the three brain anatomical atlases used in our study.

ure 4.6) highlights strong agreements, proving that methods are comparable. Also the overall trends between the different atlases are strongly similar. However considering individual networks and performing the average across individual network measures, gives results that exhibit greater smoothness and concordance within the three indices (Clustering Coefficient, Local Efficiency and Strength).

5.3 Future Developments

One of the main limitations regarding our study was that PET and MR data came from a different pool of subjects, not allowing us to have intra-subject comparison. To overcome the problem we run our analysis at population level. In addition, although R-fMRI and dMRI data came from the same subjects, we followed different analysis pathways, leading us to consider the two datasets as independent.

Future studies should aim to replicate the results of this work at individual level, where all the different imaging modalities are acquired from the same group of subjects. However one should take into account that PET studies, especially the ones involving L-[1-^{11}C]Leucine, are very complicated to be performed. Moreover, guidelines on maximum radiation exposure constraint the inclusion of the same subject in more than one PET study. This limits the availability of both L-[1-^{11}C]Leucine and [^{18}F]FDG imaging data from the same participant.

Appendix A

Appendix

A.1 Brain anatomical atlases

We report the lookup tables for the atlases we used in this study, in Table A.1 are the AAL regions, and in Table A.2 are the FreeSurfer regions. As explained in section 3.1, Craddock atlas is generated by clustering, and therefore ROIs will not correspond to anatomical regions with a proper name.

1	Precentral_L	27	HP_pHP_L	53	Caudate_L
2	Precentral_R	28	HP_pHP_R	54	Caudate_R
3	Rolandic_Oper_L	29	Amygdala_L	55	Putamen_L
4	Rolandic_Oper_R	30	Amygdala_R	56	Putamen_R
5	Supp_Motor_Area_L	31	Calcarine_L	57	Pallidum_L
6	Supp_Motor_Area_R	32	Calcarine_R	58	Pallidum_R
7	Olfactory_L	33	Cuneus_L	59	Thalamus_L
8	Olfactory_R	34	Cuneus_R	60	Thalamus_R
11	Frontal_Sup_L	35	Lingual_L	61	Heschl_L
12	Frontal_Sup_R	36	Lingual_R	62	Heschl_R
13	Frontal_Mied_L	37	Occipital_L	63	Parietal_L
14	Frontal_Mied_R	38	Occipital_R	64	Parietal_R
15	Frontal_Inf_L	39	Fusiform_L	65	Temporal_L
16	Frontal_Inf_R	40	Fusiform_R	66	Temporal_R
17	Rectus_L	41	Postcentral_L	67	Vermis
18	Rectus_R	42	Postcentral_R	68	Cerebellum_Crus_L
19	Insula_L	45	SupraMarginal_L	69	Cerebellum_Crus_R
20	Insula_R	46	SupraMarginal_R	70	Cerebellum_L
21	Cingulum_Ant_L	47	Angular_L	71	Cerebellum_R
22	Cingulum_Ant_R	48	Angular_R		
23	Cingulum_Mid_L	49	Precuneus_L		
24	Cingulum_Mid_R	50	Precuneus_R		
25	Cingulum_Post_L	51	Paracentral_Lobule_L		
26	Cingulum_Post_R	52	Paracentral_Lobule_R		

TABLE A.1: Automated Anatomical Labeling atlas lookup table

A.2 Frequency bands

In Table A.3 are reported cut-off frequencies of the bandpass filters we applied to R-fMRI data.

A.3 Complex network measures

Network indices were computed with Brain Connectivity Toolbox, which implements the following formulas, for more details see (Rubinov and Sporns, 2010).

Basic concepts and notation: N is the set of all nodes in the network, and n

10	L-Thalamus-Proper	1016	L-parahippocampal	2010	R-isthmuscingulate
11	Left-Caudate	1017	L-paracentral	2011	R-lateraloccipital
12	L-Putamen	1018	L-parsopercularis	2012	R-lateralorbitofrontal
13	L-Pallidum	1019	L-parsorbitalis	2013	R-lingual
17	L-Hippocampus	1020	L-parstriangularis	2014	R-medialorbitofrontal
18	L-Amygdala	1021	L-pericalcarine	2015	R-middletemporal
26	L-Accumbens-area	1022	L-postcentral	2016	R-parahippocampal
49	R-Thalamus-Proper	1023	L-posteriorcingulate	2017	R-paracentral
50	R-Caudate	1024	L-precentral	2018	R-parsopercularis
51	R-Putamen	1025	L-precuneus	2019	R-parsorbitalis
52	R-Pallidum	1026	L-rostralanteriorcingulate	2020	R-parstriangularis
53	R-Hippocampus	1027	L-rostralmiddlefrontal	2021	R-pericalcarine
54	R-Amygdala	1028	L-superiorfrontal	2022	R-postcentral
58	R-Accumbens-area	1029	L-superiorparietal	2023	R-posteriorcingulate
1001	L-bankssts	1030	L-superiortemporal	2024	R-precentral
1002	L-caudalanteriorcingulate	1031	L-supramarginal	2025	R-precuneus
1003	L-caudalmiddlefrontal	1032	L-frontalpole	2026	R-rostralanteriorcingulate
1005	L-cuneus	1033	L-temporalpole	2027	R-rostralmiddlefrontal
1006	L-entorhinal	1034	L-transversetemporal	2028	R-superiorfrontal
1007	L-fusiform	1035	L-insula	2029	R-superiorparietal
1008	L-inferiorparietal	2001	R-bankssts	2030	R-superiortemporal
1009	L-inferiortemporal	2002	R-caudalanteriorcingulate	2031	R-supramarginal
1010	L-isthmuscingulate	2003	R-caudalmiddlefrontal	2032	R-frontalpole
1011	L-lateraloccipital	2005	R-cuneus	2033	R-temporalpole
1012	L-lateralorbitofrontal	2006	R-entorhinal	2034	R-transversetemporal
1013	L-lingual	2007	R-fusiform	2035	R-insula
1014	L-medialorbitofrontal	2008	R-inferiorparietal		
1015	L-middletemporal	2009	R-inferiortemporal		

TABLE A.2: FreeSurfer atlas lookup table

band n°	low cut	high cut
1	0.001	0.031
2	0.021	0.051
3	0.041	0.071
4	0.061	0.091
5	0.081	0.111
6	0.101	0.131
7	0.121	0.151
8	0.141	0.171
9	0.161	0.191
10	0.181	0.211
11	0.201	0.260
12	0.241	0.300
13	0.281	0.340
14	0.321	0.380
15	0.361	0.420
16	0.401	0.460
17	0.441	0.500
18	0.481	0.540
19	0.521	0.580
20	0.561	0.620

TABLE A.3: R-fMRI filtering bands, values in Hz

is the number of nodes. L is the set of all links in the network, and l is number of links. (i, j) is a link between nodes i and j, $(i, j \in N)$. Links (i, j) are associated with connection weights w_{ij}. All the superscript w found below are reported to remark we worked with the weighted version of network indices, we reported the them to be consistent with the reference paper (Rubinov and Sporns, 2010) and literature in general.

Shortest path length: $d_{ij}^w = \sum_{a_{uv} \in g_{i \leftrightarrow j}^w} f(w_{uv})$ where f is a map (e.g., an inverse) from weight to length and $g_{i \leftrightarrow j}^w$ is the shortest weighted path between i and j.

Modularity: $Q^w = \frac{1}{l^w} \sum_{i,j \in N} \left[w_{ij} - \frac{k_i^w k_j^w}{l^w} \right] \delta_{m_i, m_j}$, where m_i is the module containing node i, and $\delta_{m_i, m_j} = 1$ if $m_i = m_j$, and 0 otherwise.

- **Betweenness Centrality** $b_i = \frac{1}{(n-1)(n-2)} \sum_{h,j \in N, h \neq j, h \neq i, j \neq i} \frac{\rho_{hj}(i)}{\rho_{hj}}$, where ρ_{hj} is the number of shortest paths between h and j, and $\rho_{hj}(i)$ is the number of shortest paths between h and j that pass through i.
- **Clustering Coefficient** $C^w = \frac{1}{n} \sum_{i \in N} \frac{2t_i^w}{k_i(k_i - 1)}$.
- **Local Efficiency** $E_{loc}^w = \frac{1}{2} \sum_{i \in N} \frac{\sum_{j,h \in N, j \neq i} \left(w_{ij} w_{ih} \left[d_{jh}^w(N_i) \right]^{-1} \right)^{1/3}}{k_i(k_i - 1)}$, where $d_{jh}^w(N_i)$ is the length of the shortest path between j and h, that contains only neighbours of i.
- **Strength** $k_i^w = \sum_{j \in N} w_{ij}$.
- **Participation coefficient** $y_i^w = 1 - \sum_{m \in M} \left(\frac{k_i^w(m)}{k_i^w} \right)^2$ where M is the set of modules (see Modularity above), and $k_i^w(m)$ is the number of links between i and all nodes in module m.
- **Within-module Degree z-score** $z_i^w = \frac{k_i^w(m_i) - \bar{k}^w(m_i)}{\sigma^{k^w(m_i)}}$ where m_i is the module containing node i, $k_i^w(m_i)$ is the within-module degree of i (the number of links between i and all other nodes in m_i), and $\bar{k}^w(m_i)$ and $\sigma^{k^w(m_i)}$ are the respective mean and standard deviation of the within-module m_i degree distribution.

A.4 Complete results

In Figures A.1, A.2, and A.3, we report correlations respectively between R-fMRI network measures and: structural network measures, [^{18}F]FDG SUV, and rCPS plus covariates (glucose metabolism, ROIs dimension and power distribution). Results are for all the 20 filtering bands and all the network indices (bc: Betweenness Centrality, cc: Clustering Coefficient, le: Local Efficiency, s: Strength, pc: Participation Coefficient, wd: Within-module Degree z-score), and as usual for the three different atlases.

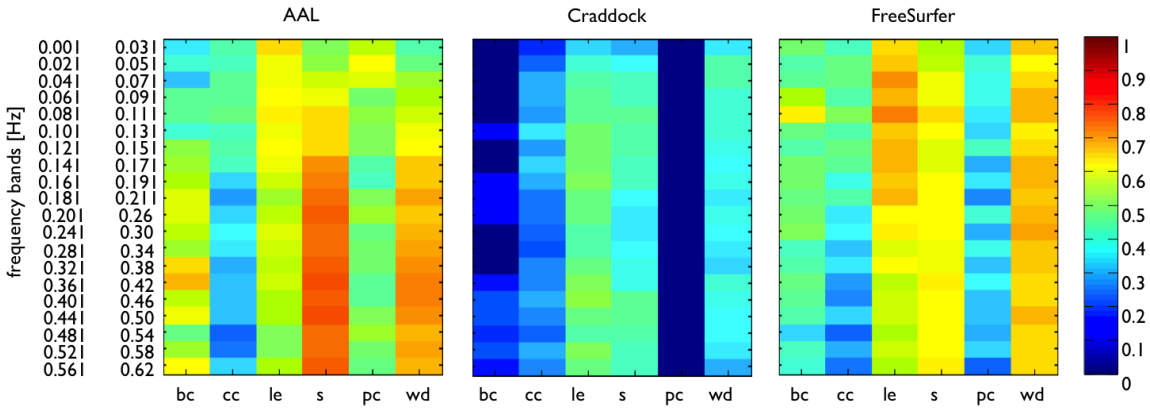

FIGURE A.1: R values between functional and structural network measures. The dependence on the R-fMRI filtering band is shown.

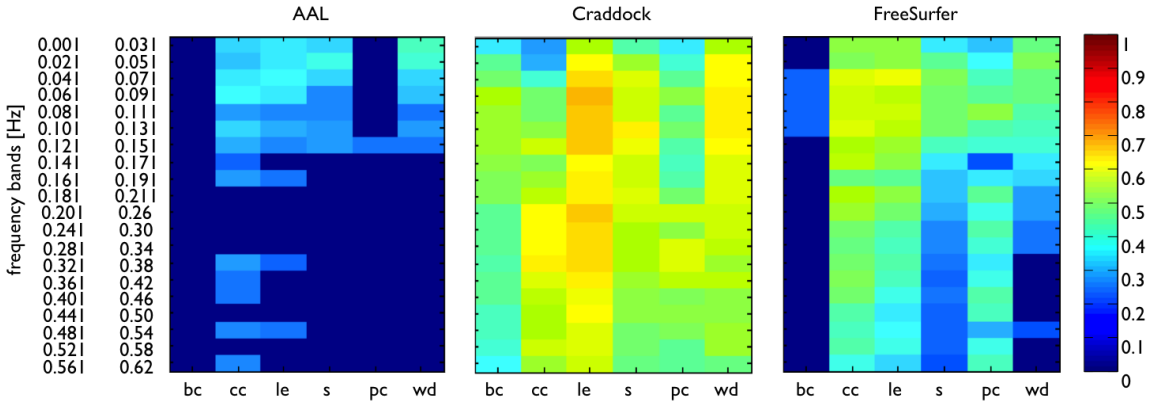

FIGURE A.2: Correlations between functional network measures and [^{18}F]FDG PET.

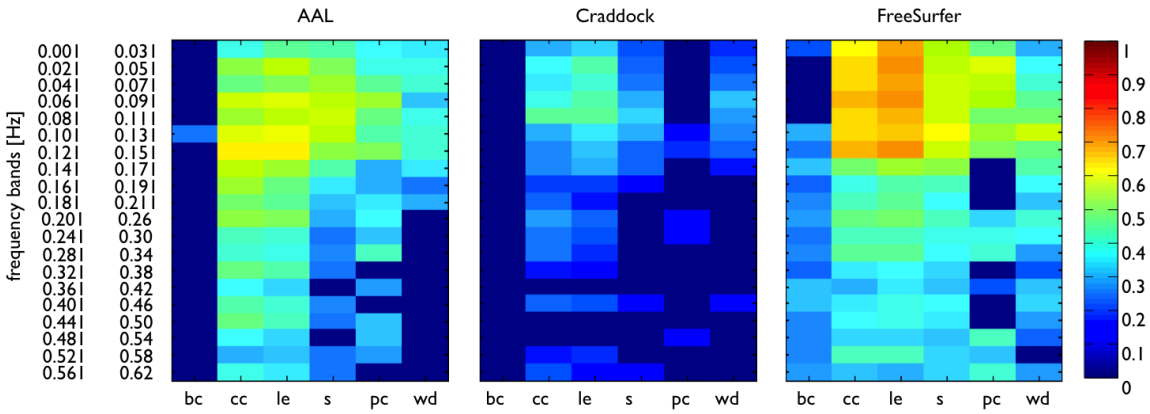

FIGURE A.3: Partial correlations between functional network measures and Leucine PET, using as covariates: FDG PET, ROIs dimension and power distribution across ROIs.

A.5 Goodness of fit

We report indices that describe the goodness of fit for the 3rd degree polynomial interpolation reported in section 4.3.2 and showed in Figure 4.6. Table A.4 reports abbreviations that stand for:

- sse: Sum of squares due to error
- rsquare: R^2 (coefficient of determination)
- adjrsquare: Degree-of-freedom adjusted coefficient of determination
- rmse: Root mean squared error (standard error)

		Clustering Coefficient	**Local Efficiency**	**Strength**
AAL	sse	0,015	0,021	0,005
	rsquare	0,728	0,657	0,965
	adjrsquare	0,627	0,528	0,951
	rmse	0,043	0,051	0,024
Craddock	sse	0,013	0,008	0,008
	rsquare	0,738	0,916	0,871
	adjrsquare	0,640	0,885	0,823
	rmse	0,040	0,031	0,032
FreeSurfer	sse	0,028	0,019	0,012
	rsquare	0,819	0,889	0,863
	adjrsquare	0,751	0,848	0,811
	rmse	0,059	0,049	0,038

TABLE A.4: Goodness of fit relatively to Figure 4.6 in Results chapter

Bibliography

Achard, Sophie and Edward T. Bullmore (2007). "Efficiency and Cost of Economical Brain Functional Networks". In: *PLoS Computational Biology* 3.2, e17. ISSN: 1553-734X. DOI: 10.1371/journal.pcbi.0030017. URL: http://dx.plos.org/10.1371/journal.pcbi.0030017.

Aiello, Marco et al. (2015). "Relationship between simultaneously acquired resting-state regional cerebral glucose metabolism and functional MRI: A PET/MR hybrid scanner study". In: *NeuroImage* 113, pp. 111–121. ISSN: 10538119. DOI: 10.1016/j.neuroimage.2015.03.017. URL: http://linkinghub.elsevier.com/retrieve/pii/S1053811915001986.

Bassett, Danielle S et al. (2009). "Cognitive fitness of cost-efficient brain functional networks." In: *Proceedings of the National Academy of Sciences of the United States of America* 106.28, pp. 11747–52. ISSN: 1091-6490. DOI: 10.1073/pnas.0903641106. URL: http://www.ncbi.nlm.nih.gov/pubmed/19564605.

Bishu, Shrinivas et al. (2008). "Regional rates of cerebral protein synthesis measured with L-[1-11C]leucine and PET in conscious, young adult men: normal values, variability, and reproducibility." In: *Journal of cerebral blood flow and metabolism : official journal of the International Society of Cerebral Blood Flow and Metabolism* 28.8, pp. 1502–13. ISSN: 1559-7016. DOI: 10.1038/jcbfm.2008.43. URL: http://www.pubmedcentral.nih.gov/articlerender.fcgi?artid=2775471{\&}tool=pmcentrez{\&}rendertype=abstract.

Borchardt, Viola et al. (2016). "Preprocessing strategy influences graph-based exploration of altered functional networks in Major Depression (in pres.)" In: *Human brain mapping* 1442.February, pp. 1422–1442. ISSN: 10659471. DOI: 10.1002/hbm.23111.

Bullmore, Edward T. and Olaf Sporns (2009). "Complex brain networks: graph theoretical analysis of structural and functional systems." In: *Nature reviews. Neuroscience* 10.3, pp. 186–198. ISSN: 1471-0048. DOI: 10.1038/nrn2575. URL: http://www.ncbi.nlm.nih.gov/pubmed/19190637.

Cowan, J. D. et al. (2013). "Self-organized criticality in a network of interacting neurons". In: *Journal of Statistical Mechanics: Theory and Experiment* 04, P04030. ISSN: 1742-5468. DOI: 10.1088/1742-5468/2013/04/

P04030. arXiv: 1209.3829. URL: http://iopscience.iop.org/1742-5468/2013/04/P04030.

Craddock, R. Cameron et al. (2012). "A whole brain fMRI atlas generated via spatially constrained spectral clustering". In: *Human Brain Mapping* 33.8, pp. 1914–1928. ISSN: 10659471. DOI: 10.1002/hbm.21333. URL: http://doi.wiley.com/10.1002/hbm.21333.

Deng, Zhidong and Yi Zhang (2007). "Collective behavior of a small-world recurrent neural system with scale-free distribution". In: *IEEE Transactions on Neural Networks* 18.5, pp. 1364–75. ISSN: 1045-9227. DOI: 10.1109/TNN.2007.894082. URL: http://www.ncbi.nlm.nih.gov/pubmed/18220186.

Filler, Aaron (2009). "The History, Development and Impact of Computed Imaging in Neurological Diagnosis and Neurosurgery: CT, MRI, and DTI". In: *Nature Precedings*, pp. 1–76. ISSN: 1756-0357. DOI: 10.1038/npre.2009.3267.5.

Fischl, Bruce (2012). "FreeSurfer". In: *NeuroImage* 62.2, pp. 774–781. ISSN: 10538119. DOI: 10.1016/j.neuroimage.2012.01.021. arXiv: NIHMS150003.

Flexner, Josefa B, Louis B Flexner, and Eliot Stellar (1963). "Memory in Mice as Affected by Intracerebral Puromycin". In: *Science* 141.3575, pp. 57–59.

Friston, Karl J. et al. (1995). "Statistical parametric maps in functional imaging: A general linear approach". In: *Human Brain Mapping* 2.4, pp. 189–210. ISSN: 10659471. DOI: 10.1002/hbm.460020402.

Gawryluk, J. R., E. L. Mazerolle, and R. C N D'Arcy (2014). "Does functional MRI detect activation in white matter? A review of emerging evidence, issues, and future directions". In: *Frontiers in Neuroscience* 8.8 JUL, pp. 1–12. ISSN: 1662453X. DOI: 10.3389/fnins.2014.00239.

Ginestet, Cedric E. et al. (2011). "Brain Network Analysis: Separating Cost from Topology Using Cost-Integration". In: *PLoS ONE* 6.7, e21570. ISSN: 1932-6203. DOI: 10.1371/journal.pone.0021570. URL: http://dx.plos.org/10.1371/journal.pone.0021570.

Griffanti, Ludovica et al. (2014). "ICA-based artefact removal and accelerated fMRI acquisition for improved resting state network imaging". In: *NeuroImage* 95, pp. 232–247. ISSN: 10538119. DOI: 10.1016/j.neuroimage.2014.03.034. URL: http://linkinghub.elsevier.com/retrieve/pii/S1053811914001815.

Guo, Christine C. et al. (2012). "One-year test-retest reliability of intrinsic connectivity network fMRI in older adults". In: *NeuroImage* 61.4, pp. 1471–1483. ISSN: 10538119. DOI: 10.1016/j.neuroimage.2012.03.027. arXiv: NIHMS150003. URL: http://dx.doi.org/10.1016/j.neuroimage.2012.03.027.

Hagmann, Patric et al. (2010). "MR connectomics: Principles and challenges". In: *Journal of Neuroscience Methods* 194.1, pp. 34–45. ISSN: 01650270. DOI: 10.1016/j.jneumeth.2010.01.014. URL: http://dx.doi.org/10.1016/j.jneumeth.2010.01.014.

He, Biyu J. et al. (2010). "The temporal structures and functional significance of scale-free brain activity". In: *Neuron* 66.3, pp. 353–369. ISSN: 08966273. DOI: 10.1016/j.neuron.2010.04.020. arXiv: NIHMS150003. URL: http://dx.doi.org/10.1016/j.neuron.2010.04.020.

Hesse, Janina and Thilo Gross (2014). "Self-organized criticality as a fundamental property of neural systems". In: *Frontiers in Systems Neuroscience* 8.September, pp. 1–14. ISSN: 1662-5137. DOI: 10.3389/fnsys.2014.00166. URL: http://journal.frontiersin.org/article/10.3389/fnsys.2014.00166/abstract.

Heuvel, Martijn P. van den and Olaf Sporns (2011). "Rich-Club Organization of the Human Connectome". In: *Journal of Neuroscience* 31.44, pp. 15775–15786. ISSN: 0270-6474. DOI: 10.1523/JNEUROSCI.3539-11.2011.

Honey, Christopher J., Jean-Philippe Thivierge, and Olaf Sporns (2010). "Can structure predict function in the human brain?" In: *NeuroImage* 52.3, pp. 766–776. ISSN: 10538119. DOI: 10.1016/j.neuroimage.2010.01.071. URL: http://linkinghub.elsevier.com/retrieve/pii/S1053811910000935.

Klunk, William E et al. (2004). "Imaging Brain Amyloid in Alzheimer ' s Disease with Pittsburgh Compound-B". In: pp. 306–319. ISSN: 03645134. DOI: 10.1002/ana.20009.

Latora, V and M Marchiori (2001). "Efficient behavior of small-world networks." In: *Physical review letters* 87.19, p. 198701. ISSN: 0031-9007. DOI: 10.1103/PhysRevLett.87.198701. arXiv: 0101396 [cond-mat].

Magnasco, Marcelo O., Oreste Piro, and Guillermo A. Cecchi (2009). "Self-tuned critical anti-Hebbian networks". In: *Physical Review Letters* 102.25, pp. 1–4. ISSN: 00319007. DOI: 10.1103/PhysRevLett.102.258102. arXiv: 0808.3996.

Mapping, Human Connectome (2014). "WU-Minn HCP 500 Subjects Data Release : Reference Manual". In: June.

Massobrio, Paolo, Valentina Pasquale, and Sergio Martinoia (2015). "Self-organized criticality in cortical assemblies occurs in concurrent scale-free and small-world networks". In: *Scientific Reports* 5.October 2014, p. 10578. ISSN: 2045-2322. DOI: 10.1038/srep10578. URL: http://www.nature.com/doifinder/10.1038/srep10578.

Meisel, Christian and Thilo Gross (2009). "Adaptive self-organization in a realistic neural network model". In: *Physical Review E - Statistical, Nonlinear, and Soft Matter Physics* 80.6. ISSN: 15393755. DOI: 10.1103/PhysRevE.80.061917. arXiv: 0903.2987.

Monti, Ricardo Pio et al. (2014). "Estimating time-varying brain connectivity networks from functional MRI time series". In: *NeuroImage* 103, pp. 427–443. ISSN: 10959572. DOI: 10.1016/j.neuroimage.2014.07.033. arXiv: 1310.3863. URL: http://dx.doi.org/10.1016/j.neuroimage.2014.07.033.

Park, Hae-Jeong and Karl J. Friston (2013). "Structural and functional brain networks: from connections to cognition." In: *Science (New York, N.Y.)* 342.6158, p. 1238411. ISSN: 1095-9203. DOI: 10.1126/science.1238411. URL: http://www.ncbi.nlm.nih.gov/pubmed/24179229.

Ponce-Alvarez, Adri??n et al. (2015). "Resting-State Temporal Synchronization Networks Emerge from Connectivity Topology and Heterogeneity". In: *PLoS Computational Biology* 11.2, pp. 1–23. ISSN: 15537358. DOI: 10.1371/journal.pcbi.1004100.

Raichle, M E et al. (2001). "A default mode of brain function." In: *Proceedings of the National Academy of Sciences of the United States of America* 98.2, pp. 676–682. ISSN: 0027-8424. DOI: 10.1073/pnas.98.2.676. arXiv: 0402594v3 [arXiv:cond-mat].

Riedl, V. et al. (2014). "Local Activity Determines Functional Connectivity in the Resting Human Brain: A Simultaneous FDG-PET/fMRI Study". In: *Journal of Neuroscience* 34.18, pp. 6260–6266. ISSN: 0270-6474. DOI: 10.1523/JNEUROSCI.0492-14.2014. URL: http://www.jneurosci.org/cgi/doi/10.1523/JNEUROSCI.0492-14.2014.

Rubinov, Mikail and Olaf Sporns (2010). "Complex network measures of brain connectivity: uses and interpretations." In: *NeuroImage* 52.3, pp. 1059–69. ISSN: 1095-9572. DOI: 10.1016/j.neuroimage.2009.10.003. URL: http://www.sciencedirect.com/science/article/pii/S105381190901074X.

Rubinov, Mikail et al. (2011). "Neurobiologically realistic determinants of Self-Organized criticality in networks of spiking neurons". In: *PLoS Computational Biology* 7.6. ISSN: 1553734X. DOI: 10.1371/journal.pcbi.1002038.

Salimi-Khorshidi, Gholamreza et al. (2014). "Automatic denoising of functional MRI data: Combining independent component analysis and hierarchical fusion of classifiers". In: *NeuroImage* 90, pp. 449–468. ISSN: 10538119. DOI: 10.1016/j.neuroimage.2013.11.046. URL: http://linkinghub.elsevier.com/retrieve/pii/S1053811913011956.

Schmidt, Kathleen C et al. (2005). "Measurement of regional rates of cerebral protein synthesis with L-[1-11C]leucine and PET with correction for recycling of tissue amino acids: I. Kinetic modeling approach." In: *Journal of cerebral blood flow and metabolism : official journal of the International Society of Cerebral Blood Flow and Metabolism* 25.5, pp. 617–28.

ISSN: 0271-678X. DOI: 10.1038/sj.jcbfm.9600067. URL: http://www.ncbi.nlm.nih.gov/pubmed/15703696.

Skudlarski, Pawel et al. (2008). "Measuring brain connectivity: Diffusion tensor imaging validates resting state temporal correlations". In: *NeuroImage* 43.3, pp. 554–561. ISSN: 10538119. DOI: 10.1016/j.neuroimage.2008.07.063. URL: http://dx.doi.org/10.1016/j.neuroimage.2008.07.063.

Smith, Carolyn Beebe et al. (2005). "Measurement of regional rates of cerebral protein synthesis with L-[1-11C]leucine and PET with correction for recycling of tissue amino acids: II. Validation in rhesus monkeys". In: *Journal of cerebral blood flow and metabolism : official journal of the International Society of Cerebral Blood Flow and Metabolism* 25.5, pp. 629–40. ISSN: 0271-678X. DOI: 10.1038/sj.jcbfm.9600067. URL: http://www.ncbi.nlm.nih.gov/pubmed/15703696.

Smith, Robert E. et al. (2013). "SIFT: Spherical-deconvolution informed filtering of tractograms". In: *NeuroImage* 67.DECEMBER, pp. 298–312. ISSN: 10538119. DOI: 10.1016/j.neuroimage.2012.11.049.

Sotiropoulos, Stamatios N. et al. (2013). "Advances in diffusion MRI acquisition and processing in the Human Connectome Project". In: *NeuroImage* 80, pp. 125–143. ISSN: 10538119. DOI: 10.1016/j.neuroimage.2013.05.057. URL: http://linkinghub.elsevier.com/retrieve/pii/S105381191300551X.

Sporns, Olaf and Martijn P. van den Heuvel (2013). "Network maps of the human brain's rich club". In: *Network Science* 1.02, pp. 248–250. ISSN: 2050-1242. DOI: 10.1017/nws.2013.8. URL: http://www.journals.cambridge.org/abstract{_}S2050124213000088.

Sporns, Olaf, G Tononi, and G M Edelman (2000). "Theoretical neuroanatomy: relating anatomical and functional connectivity in graphs and cortical connection matrices." In: *Cerebral cortex (New York, N.Y. : 1991)* 10.2, pp. 127–141. ISSN: 1047-3211. DOI: 10.1093/cercor/10.2.127.

Sporns, Olaf and Jonathan D Zwi (2004). "The small world of the cerebral cortex." In: *Neuroinformatics* 2.2, pp. 145–162. ISSN: 1539-2791. DOI: 10.1385/NI:2:2:145.

Tomasi, Dardo, Gj Wang, and Nd Volkow (2013). "Energetic cost of brain functional connectivity". In: *Proceedings of the National Academy of Sciences* 110, pp. 13642–13647. ISSN: 0027-8424. DOI: 10.1073/pnas.1303346110/-/DCSupplemental.www.pnas.org/cgi/doi/10.1073/pnas.1303346110. URL: http://www.pnas.org/content/110/33/13642.short.

Tournier, J-D., F. Calamante, and A. Connelly (2010). "Improved probabilistic streamlines tractography by 2 nd order integration over fibre orientation distributions". In: *Ismrm* 88.2003, p. 2010.

Tzourio-Mazoyer, N et al. (2002). "Automated anatomical labeling of activations in SPM using a macroscopic anatomical parcellation of the MNI MRI single-subject brain." In: *NeuroImage* 15.1, pp. 273–289. ISSN: 1053-8119. DOI: 10.1006/nimg.2001.0978.

Van Essen, David C. et al. (2013). "The WU-Minn Human Connectome Project: An overview". In: *NeuroImage* 80, pp. 62–79. ISSN: 10538119. DOI: 10.1016/j.neuroimage.2013.05.041. arXiv: NIHMS150003. URL: http://dx.doi.org/10.1016/j.neuroimage.2013.05.041.

Veronese, Mattia et al. (2010). "A spectral analysis approach for determination of regional rates of cerebral protein synthesis with the L-[1-(11)C]leucine PET method." In: *Journal of cerebral blood flow and metabolism : official journal of the International Society of Cerebral Blood Flow and Metabolism* 30.8, pp. 1460–1476. ISSN: 0271-678X. DOI: 10.1038/jcbfm.2010.26. URL: http://dx.doi.org/10.1038/jcbfm.2010.26.

Veronese, Mattia et al. (2012). "Use of spectral analysis with iterative filter for voxelwise determination of regional rates of cerebral protein synthesis with L-[1-11C]leucine PET." In: *Journal of cerebral blood flow and metabolism : official journal of the International Society of Cerebral Blood Flow and Metabolism* 32.6, pp. 1073–85. ISSN: 1559-7016. DOI: 10.1038/jcbfm.2012.27. URL: http://www.ncbi.nlm.nih.gov/pubmed/22395209.

Veronese, Mattia et al. (2015). "Quantification of [11C]PIB PET for imaging myelin in the human brain: a test–retest reproducibility study in high-resolution research tomography". In: *Journal of Cerebral Blood Flow & Metabolism* April, pp. 1–12. ISSN: 0271-678X. DOI: 10.1038/jcbfm.2015.120. URL: http://www.nature.com/doifinder/10.1038/jcbfm.2015.120.

Welton, Thomas et al. (2015). "Reproducibility of Graph-Theoretic Brain Network Metrics: A Systematic Review". In: *Brain Connectivity* 5.4, pp. 193–202. ISSN: 2158-0014. DOI: 10.1089/brain.2014.0313. URL: http://online.liebertpub.com/doi/10.1089/brain.2014.0313.

Wienhard, K. et al. (2002). "The ECAT HRRT : Performance and First Clinical Application of the New High Resolution Research Tomograph". In: *IEEE Transactions on Nuclear Science* 49.1, pp. 104–110. ISSN: 0018-9499. DOI: 10.1109/TNS.2002.998689. URL: http://ieeexplore.ieee.org/xpls/abs{_}all.jsp?arnumber=998689{\&}tag=1.

Zuo, Xi Nian et al. (2012). "Network centrality in the human functional connectome (HUBS)". In: *Cerebral Cortex* 22.8, pp. 1862–1875. ISSN: 10473211. DOI: 10.1093/cercor/bhr269.